Icarus 439 (2025) 116630

Contents lists available at ScienceDirect

Icarus

journal homepage: www.elsevier.com/locate/icarus

Research Paper

The influence of spin–orbit resonances on the evolution of Mercury's mantle and crust

Nicola Tosi [a,*], Falko Schulz [a], Michaela Walterová [b], Sebastiano Padovan [c]

[a] German Aerospace Center (DLR), Institute of Space Research, Rutherford Strasse 2, Berlin, 12489, Germany
[b] Charles University, Faculty of Mathematics and Physics, Department of Geophysics, V Holešovičkách 2, Prague 8, 180 00, Czech Republic
[c] European Organisation for the Exploitation of Meteorological Satellites (EUMETSAT), Eumetsat Allee 1, Darmstadt, 64295, Germany

ARTICLE INFO

Dataset link: https://zenodo.org/records/15484924

Keywords:
Mercury
Spin–orbit resonance
Mantle convection
Crust
Radial contraction

ABSTRACT

Mercury's record of large impact basins and spin evolution models suggest that its present-day 3:2 spin–orbit resonance may not be primordial. It could have been established up to hundreds of millions of years after planet formation, possibly triggered by the impact that created the Caloris basin about 3.7 billion years ago. Before this, Mercury may have been in a synchronous rotation or a 2:1 resonance, which would have induced strong hemispheric surface temperature variations, influencing the thermal structure of the lithosphere and mantle.

Using 3D thermochemical mantle convection models, we simulate Mercury's mantle evolution and volcanic crust formation over one billion years, incorporating surface temperature distributions from different spin–orbit resonances. We assess whether these variations can generate large-scale lateral differences in crustal thickness, as inferred from gravity, topography and surface composition data, and compare predicted radius changes due to mantle and core cooling with existing estimates from compressional tectonic features.

Crustal thickness, interior cooling rate, and radius change are primarily controlled by internal heat production, with models using intermediate to high heat production rates (characteristic of CI and EH chondrites) best matching observations. The mantle reference viscosity, low thermal conductivity attained at Mercury's mantle conditions, and cooling due to melt extraction exert first-order controls on the timing of crust emplacement and its final extent. Regardless of surface temperature patterns, mantle convection is dominated by small, stable cells. While surface temperature variations influence the location of hot and cold regions at large scales, they do not alter the spatial scale of convection. Assuming vertical melt extraction, crustal thickness locally follows the convection pattern. The present-day 3:2 resonance does not induce significant large-scale variations in crustal thickness, but a past synchronous rotation could have produced hemispheric differences, with crust up to 10–15 km thicker on the dayside. Similarly, radial contraction is hemispherical, with the hot hemisphere contracting less and at a slower rate than the cold one as long as the resonance persists.

The surface record does not clearly support these hemispheric patterns. This suggests that past spin–orbit resonances may have been short lived, or that they may have affected Mercury's interior more subtly than our models predict, or that subsequent geological processes erased or modified early large-scale asymmetries. Future high-resolution imaging and surface composition data from BepiColombo, particularly of Mercury's poorly-mapped southern hemisphere, will be critical in testing this hypothesis and in refining the available constraints on the planet's crustal evolution and tectonic history.

1. Introduction

1.1. Constraints on mercury's crust

The bulk of Mercury's crust is likely secondary, being the result of volcanism induced by partial melting of the convective solid mantle during the planet's early evolution (e.g., Denevi et al., 2013). A primary crust may have formed through the flotation of buoyant graphite in a crystallizing magma ocean as inferred from the widespread presence of carbon-rich low-reflectance materials on the planet's surface (Vander Kaaden and McCubbin, 2015; Peplowski et al., 2016; Klima et al.,

* Corresponding author.
E-mail address: nicola.tosi@dlr.de (N. Tosi).

https://doi.org/10.1016/j.icarus.2025.116630
Received 15 February 2025; Received in revised form 7 April 2025; Accepted 28 April 2025
Available online 21 May 2025

2018; Lark et al., 2023). The thickness of this carbon-rich crust strongly depends on the carbon content of the primitive mantle, which is not well unconstrained. For carbon contents similar to the Earth or Mars, it would only amount to up to a few hundred meters (Vander Kaaden and McCubbin, 2015), but it could reach several km if, upon formation, Mercury was saturated in carbon (Lark et al., 2023).

Gravity and topography data are routinely used to estimate the thickness of the secondary crust on terrestrial planets (Wieczorek, 2015), and Mercury makes no exception. The average crustal thickness estimated from these data varies widely, from 26 ± 11 km (Sori, 2018), up to 35 ± 18 km (Padovan et al., 2015), or possibly even higher (e.g., Smith et al., 2012; Beuthe et al., 2020), although in the latter cases the average thickness only represents an essentially unconstrained reference value with respect to which undulations of the crust-mantle interface are calculated. Overall, the average thickness of Mercury's crust could be anywhere between about 15 and 60 km. The time over which such a secondary crust was emplaced and the rate at which this took place are also not well constrained. Yet, it is reasonable to expect that the phase of crust production coincided with the period of widespread effusive volcanism, which ended around 3.5 Ga (Byrne et al., 2016). The bulk of Mercury's crust was thus built over a time span of about 1 Gyr.

A striking feature of Mercury's surface is the presence of large-scale heterogeneities (e.g., McCoy et al., 2018). Although remote sensing measurements from the MESSENGER mission are limited to the elemental distribution in the northern hemisphere (Nittler et al., 2011; Weider et al., 2012, 2015; Peplowski and Stockstill-Cahill, 2019), the accompanying heterogeneity has been petrologically interpreted as a natural consequence of a varying degree of partial melting of the (possibly also heterogeneous) mantle source (Charlier et al., 2013; Namur et al., 2016; Namur and Charlier, 2017). Beuthe et al. (2020), using a lateral distribution of the surface density inferred from melting experiments suggested that gravity and topography data imply large-scale variations of the crustal thickness, which can also be interpreted as the result of a laterally-varying degree of mantle melting (Fig. 1). Particularly noteworthy is the case of the so-called high-Mg region (Weider et al., 2015; McCoy et al., 2018), a large area ($>5{\cdot}10^6$ km^2) having by far the highest Mg/Si ratio of the sampled surface. When lateral variations in density are not considered, this area is not associated with any significant crustal thickness anomaly (model U0 by Beuthe et al. (2020) shown in Fig. 1a). However, according to the analysis of Beuthe et al. (2020), the high-Mg region is expected to be anomalously dense and, as a consequence, to be underlain by a remarkably thick crustal root. For their nominal model with a mean reference crustal thickness of 35 km, the inferred crust beneath the high-Mg region is 50 ± 12 km thick, with peak values as high as ~100 km (model V0 in Fig. 1b), or even higher when a mean crustal thickness of 45 km is assumed (model V4 in Fig. 1c).

Despite large uncertainties, the thickness of the crust and the timing of its production have long been considered important elements to constrain models of the thermal evolution of terrestrial planets in general, and of Mercury in particular (e.g., Hauck et al., 2004; Breuer et al., 2007; Grott et al., 2011; Tosi et al., 2013; Hauck et al., 2018; Peterson et al., 2021; Tosi and Padovan, 2021; Xie et al., 2022). These models, most of which are based on simplified one-dimensional, so-called "parameterized" thermal evolution codes, are typically successful at reproducing the expected range of the average crustal thickness as well as its timing. Despite the above efforts, little attention has been devoted so far to satisfy the crustal constraints with more sophisticated two- or three-dimensional models where the local – rather than global – treatment of melting can provide better insights into the amount and timing of crustal production. Furthermore, 1D thermal evolution models can only be used to reproduce the bulk volume of the crust and not its lateral variations.

In this work, we use 3D models of the first billion year of the thermochemical evolution of Mercury with the goal of understanding to what extent lateral heterogeneities resulting from mantle convection can be responsible for the expected variability of the crustal thickness.

1.2. Possible role of early spin–orbit resonances on crust formation

Previous purely thermal models have shown that the convection planform in Mercury's thin mantle is characterized by stable, small-scale cells of nearly unitary aspect ratio (Michel et al., 2013; Tosi et al., 2013, 2015; Guerrero et al., 2021). If melting occurs, as expected, in hot upwellings reaching the base of the lithosphere, we can anticipate that the crust distribution will reflect the small-scale planform of mantle convection, which is at odds with the inferred existence of large-scale crustal heterogeneities. In the search for a possible mechanism that could affect the convection planform and produce heterogeneities at the relevant spatial scales (>2000–3000 km if one considers, for example, the high-Mg region), we study here the influence on crust production of the present-day 3:2 spin–orbit resonance and of putative early orbital resonances different from the current one. In fact, on an airless body like Mercury, low-order resonances such as 1:1 (synchronous rotation) or 2:1 are accompanied by lateral variations of the surface temperature in excess of several hundred degrees (see Section 3). These may affect the temperature of the deep mantle and in turn melting and crust production to a greater extent than those of ~250 K associated with the current 3:2 resonance (Vasavada et al., 1999), which have previously been shown to affect the low-degree geoid and shape (Tosi et al., 2015) and the distribution of the elastic lithosphere thickness and present-day surface heat flux (Fleury et al., 2024).

When exactly Mercury was captured in its 3:2 resonance is still a matter of debate. Wieczorek et al. (2012) showed that Mercury would be captured with a high probability into a synchronous (1:1) resonance if it was initially in a retrograde rotation. In fact, $N-$body simulations suggest that, due to the stochastic nature of giant impacts during the final stages of planet formation, the obliquity distribution of planets is isotropic, i.e., it can range from 0° to 180° (Agnor et al., 1999; Kokubo and Ida, 2007; Miguel and Brunini, 2010), making a retrograde rotation equally likely as a prograde rotation. A late, high-energetic impact such as the one at ~3.7 Ga that formed the Caloris basin (Le Feuvre and Wieczorek, 2011; Orgel et al., 2020) could have eventually disrupted the synchronous state causing the planet to attain its current resonance (Correia and Laskar, 2012; Wieczorek et al., 2012). Wieczorek et al. (2012) further substantiated this hypothesis by showing that the spatial distribution of large impact basins is actually best explained by a prolonged synchronous rotation. Tosi et al. (2015) showed that the deformation induced by the elastic response of the lithosphere to the present-day (3:2) pattern of insolation can explain the strong departure of Mercury's long-wavelength gravity and shape from hydrostatic equilibrium only for a limited range of thickness of the elastic lithosphere. Thermal evolution models suggest that such a thickness must have been achieved later than about 1 Gyr after planet formation, thus supporting the theory of Wieczorek et al. (2012) of a late capture into the current resonance. By contrast, Noyelles et al. (2014), using an orbital model with an improved treatment of the viscoelastic tidal response and core-mantle coupling, argued against the above hypothesis, showing that an early capture into a 3:2 resonance is actually very likely, although lower resonances such as 1:1 or 2:1 may also have occurred with non-negligible probability. Later, Knibbe and van Westrenen (2017) re-evaluated the issue focusing on the distribution of large basins and its compatibility with different orbital resonances. They showed that, for a given resonance, the expected basin distribution strongly depends on assumptions on the population of impactors present in the early inner solar system, which is difficult to constrain. Yet, they concluded that the observed basin distribution cannot be explained if the planet was in a 3:2 spin–orbit resonance at the time of basin formation, but it can be well explained if it was instead in a 1:1 or 2:1 resonance. Knibbe and van Westrenen (2017) also showed that the Caloris-forming impact is actually the only one that could have imparted sufficient momentum to directly spin-up a synchronously-rotating Mercury into the present 3:2 state. But they also observed that a 2:1 resonance can be easily destabilized by many

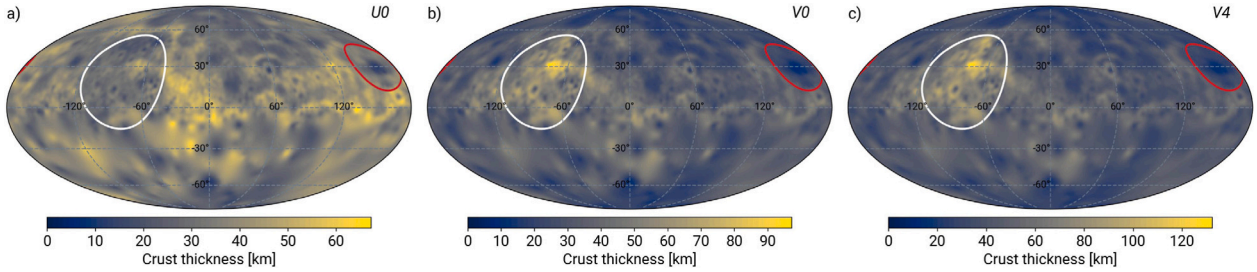

Fig. 1. Reproduction of crustal thickness maps obtained by Beuthe et al. (2020) from gravity, topography and surface composition data. (a) Model U0, which assumes a uniform crustal density and a mean crustal thickness of 35 km; (b) model V0, which assumes a laterally-variable crustal density based on the surface abundance of major elements and a mean crustal thickness of 35 km; (c) model V4, which is as model V0 but assumes a higher mean crustal thickness of 45 km. The white line corresponds to a circle with a radius of 1500 km that roughly encompasses the high-Mg region. The red circle is drawn for reference and corresponds to the Caloris basin with a radius of 750 km.

smaller impacts of which there is evidence at the surface, arguing that this may actually be a more plausible scenario.

Large variations in surface temperature can have a strong influence on the dynamics of the mantle and on the localization of hot plumes and cold downwellings as shown by mantle convection models of tidally-locked exoplanets (e.g., Van Summeren et al., 2011; Meier et al., 2024). In order to assess the influence of the insolation associated with different orbital resonances on the early evolution of Mercury and on the production of its crust, we carry out 3D simulations of thermochemical convection considering as boundary conditions the surface temperature distribution associated with the resonances 3:2, 2:1 and 1:1 (Section 2.5).

2. Methods

2.1. Governing equations

We use our mantle convection code GAIA (Hüttig et al., 2013) to perform a series of 3D simulations of the thermochemical evolution of Mercury over the first 1 Gyr. Since we are interested here in the phase during which the bulk of the secondary crust was produced, this relatively short time span is sufficient for our purposes.

We solve the conservation equations of mass, linear momentum, and thermal energy in a 3D spherical shell under the extended Boussinesq approximation (e.g., Christensen and Yuen., 1984; King et al., 2010), which is appropriate given the limited effect of compressibility in Mercury's thin mantle. In non-dimensional form, with primed quantities indicating non-dimensional variables, these read respectively:

$$\boldsymbol{\nabla}' \cdot \boldsymbol{u}' = 0, \tag{1}$$

$$-\boldsymbol{\nabla}' p' + \boldsymbol{\nabla}' \cdot \left(\eta' \left(\boldsymbol{\nabla}' \boldsymbol{u}' + \boldsymbol{\nabla}'^{\mathrm{T}} \boldsymbol{u}' \right) \right) = Ra\, \alpha'\, T' \boldsymbol{e}_r, \tag{2}$$

$$\frac{\partial T'}{\partial t'} + \boldsymbol{u}' \cdot \boldsymbol{\nabla}' T' = \boldsymbol{\nabla}' \cdot \left(k' \boldsymbol{\nabla}' T' \right) + Di\, \alpha'\, u_r' \left(T' + T_s' \right) + \frac{Di}{Ra} \Phi' + \frac{Ra_Q}{Ra}, \tag{3}$$

where $\boldsymbol{u}'$ is the flow velocity and u_r' its radial component, p' is the dynamic pressure, T' is the temperature and T_s' its surface value, $\boldsymbol{e}_r$ is the unit radial vector, and $\Phi' = (\boldsymbol{\tau}' : \boldsymbol{\epsilon}')/2$ is the viscous dissipation, with $\boldsymbol{\tau}'$ and $\boldsymbol{\epsilon}'$ the deviatoric stress tensor and strain-rate tensor, respectively. The viscosity (η'), thermal conductivity (k') and thermal expansivity (α') can depend on temperature and depth (Section 2.3). In Eqs. (1)–(3), three non-dimensional numbers appear, namely the thermal Rayleigh number

$$Ra = \frac{\rho_m^2 c_{p,m} g \alpha_r \Delta T_0 D^3}{\eta_r k_r}, \tag{4}$$

the internal heating Rayleigh number

$$Ra_Q = \frac{\rho_m^3 c_{p,m} g \alpha_r H D^5}{\eta_r k_r^2}, \tag{5}$$

and the dissipation number

$$Di = \frac{\alpha_r g D}{c_{p,m}}. \tag{6}$$

In Eqs. (4)–(6), ρ_m is the mantle density, g is the gravity acceleration (assumed to be constant throughout the mantle), $c_{p,m}$ is the mantle heat capacity, and D is the mantle thickness. The (dimensional) reference values of viscosity (η_r), thermal conductivity (k_r), and thermal expansivity (α_r) are set at a reference temperature T_r and at a reference hydrostatic pressure P_r (see Section 2.3). ΔT_0 is the temperature drop from the initial core–mantle boundary (CMB) temperature ($T_{c,0} = T_c(t = 4.55\ \mathrm{Ga})$) to the minimum value of the surface temperature (Section 2.5). Finally, H is the time- and composition-dependent internal heat production due to decaying radioactive sources (Section 2.2). Table 1 contains numerical values of the parameters introduced above, as well as of several more that are introduced below and in the subsequent sections.

Eqs. (1)–(3) are supplemented by a standard equation for the evolution of the core temperature (T_c), which assumes the core to be fully convective and, in dimensional form, reads:

$$\rho_c c_{p,c} V_c \frac{dT_c}{dt} = -A_c\, q_c, \tag{7}$$

where ρ_c is the core density, $c_{p,c}$ is the core specific heat capacity, V_c is the core volume, A_c is the surface area of the CMB, q_c is the mean heat flux across the CMB, i.e.

$$q_c = k \left. \frac{\partial \overline{T}(r)}{\partial r} \right|_{r=R_c^+}, \tag{8}$$

where k is the thermal conductivity of the mantle above the CMB, r is the radial coordinate, R_c^+ is the core radius (the + indicates that the temperature gradient is taken on the mantle side of the boundary), and $\overline{T}$ is the laterally-averaged temperature profile. For simplicity, we neglect core freezing and the formation of a stable conductive layer beneath the CMB, both of which can cause the CMB temperature to decrease more slowly than under our assumption of a fully convective core (Knibbe and van Westrenen, 2018; Knibbe and Van Hoolst, 2021; Davies et al., 2024). The implication for our models is that they may underestimate the temperature difference between mantle and core. A larger temperature drop across the lower thermal boundary layer would cause more vigorous convection and slightly hotter plumes that could generate more melt, ultimately leading to a thicker crust, an effect that should be quantified with future dedicated models.

Table 1
Numerical values of the model parameters.

Symbol	Parameter	Value
R_p	Planet radius	2440 km
R_c	Core radius	2015, 1955 km
D	Mantle thickness	425, 485 km
g	Gravity acceleration	3.7 m/s^2
ρ_m	Mantle density[a]	3278 kg/m^3
ρ_c	Core density[a]	7116 kg/m^3
$c_{p,m}$	Mantle heat capacity	1100 J/(kg K)
$c_{p,c}$	Core heat capacity	800 J/(kg K)
α_r	Mantle thermal expansivity	$3\cdot10^{-5}$ 1/K or eq. (12)
α_0	Thermal expansivity coeff.	$3.15\cdot10^{-5}$ 1/K
α_1	Thermal expansivity coeff.[b]	$1.02\cdot10^{-8}$ 1/K^2
α_2	Thermal expansivity coeff.[b]	−0.76 K
α_3	Thermal expansivity coeff.[b]	$3.63\cdot10^{-2}$ 1/GPa
α_c	Core thermal expansivity[c]	$6\cdot10^{-5}$ 1/K
k_r	Mantle thermal conductivity	3 W/(m K) or eq. (11)
k_0	Thermal conductivity coeff.[d]	4.1 W/(m K)
k_1	Thermal conductivity coeff.[d]	0.0078 W/(m K GPa)
n_k	Thermal conductivity coeff.[d]	0.493
η_r	Reference viscosity	$5\cdot10^{20}$, 10^{21}, $5\cdot10^{21}$ Pa s
E^*	Activation energy[e]	300 kJ/mol
V^*	Activation volume[e]	$6\cdot10^{-6}$ m^3/mol
T_r	Reference temperature	1600 K
P_r	Reference pressure	3 GPa
$T_{c,0}$	Initial CMB temperature	2000 K
$T_{s,min}$	Minimum surface temperature[f]	350, 182, 167, 0 K
f	Fraction of extractable crust component	0.4
$\delta V/V$	Volume change due to differentiation	0.01
ΔT_0	Initial temperature difference[f]	1650, 1818, 1833, 2000 K
H_0	Initial heat production rate[g]	40.7, 28.7, 10.6 pW/kg

[a] From the reference model of Margot et al. (2018).
[b] From Tosi et al. (2013b).
[c] From the parametrization of Tosi et al. (2013), based on data by Li et al. (2007).
[d] From Xu et al. (2004).
[e] From Karato and Wu (1993).
[f] The four values of the minimum surface temperature and of the initial temperature difference refer respectively to cases with uniform temperature, 3:2, 2:1, and 1:1 resonance. For the last the three cases, the surface temperature corresponds to the average over one insolation period.
[g] The three values of the initial heat production refer respectively to the three HPE models EH, CI, and K-depleted EH.

2.2. Mantle melting, crust production and heat piping

In addition to the conservation equations (1)–(3), we solve an equation for the transport of composition (C')

$$\frac{\partial C'}{\partial t'} + \boldsymbol{u}' \cdot \boldsymbol{\nabla}' C' = 0. \tag{9}$$

which we treat via tracing particles (Plesa et al., 2013; Plesa and Breuer, 2014). All simulations start with a homogeneous mantle. In other words, we neglect any compositional stratification that may result from the solidification of a magma ocean. We believe this is a reasonable first-order assumption, although it should be noted that some petrological models of the purely fractional solidification of a putative Mercury's magma ocean suggest that some degree of density stratification could be expected (Brown and Elkins-Tanton, 2009; Mouser and Dygert, 2023).

Whenever the temperature in a cell of the domain exceeds the solidus, we compute an instantaneous melt fraction (ϕ) assuming its linear increase between solidus and liquidus and taking into account latent heat of melting following the approach detailed in Padovan et al. (2017). We then deplete the composition of the particles present in that cell linearly with ϕ and generate a volume of crustal material ϕV_i, where V_i is the volume of the ith cell where melting occurs. Such a volume is extracted radially to the surface to instantaneously form new crust on top of the existing one, which is then advected downward. In some simulations we additionally take into account cooling due to melt extraction and sedimentation, i.e. the so-called heat piping effect (Moore and Webb, 2013; Peterson et al., 2021). In this cases, the volume of extracted melt is used not only to "bury" existing crust, but also to downward advect the temperature field, which translates in a net cooling effect of the lithosphere and upper mantle. Practically, we treat the downward advection of temperature upon melt extraction column-by-column, which is possible since we work with a structured, projected grid (see Section 3). For each column of the domain, we determine at each timestep the cells where the temperature exceeds the solidus and calculate the corresponding volume of melt produced. In all cells overlying those where melting occurs, we then update the temperature by replacing the fraction of melt volume to cell volume with the temperature of the overlying cell.

Depleted particles that undergo melting are also associated with a solidus increase – again linear with ϕ – that renders melting of already depleted mantle progressively more difficult. We neglect density changes in the mantle upon melt extraction. In fact, given the extremely low abundance of FeO in Mercury's mantle (Nittler et al., 2011; Zolotov et al., 2013; Vander Kaaden and McCubbin, 2015), the composition of the mantle residuum is likely to have a density that is similar to that of the primordial material with little effects due to compositional buoyancy.

Finally, upon melting and crust production, we also deplete the source mantle and enrich the crust in HPE according to a constant depletion/enrichment factor, whose choice is detailed in Section 3.

2.3. Transport and thermal properties

In all simulations we assume a standard temperature- and pressure-dependent viscosity (e.g., Tosi et al., 2013; Michel et al., 2013; Padovan

et al., 2017; Guerrero et al., 2021), which we calculate according to the Arrhenius law for diffusion creep. In dimensional form this reads:

$$\eta(T,P) = \eta_r \exp\left(\frac{E^* + PV^*}{RT} - \frac{E^* + P_r V^*}{RT_r}\right), \quad (10)$$

where E^* and V^* are activation energy and activation volume, respectively, R is the gas constant, and T_r and P_r are reference temperature and pressure introduced above. Due to Mercury's thin mantle, the pressure dependence of the viscosity has only a minor effect. For example, at CMB conditions (e.g. $P = 5$ GPa and $T = 2000$ K), with our chosen activation volume of $6 \cdot 10^{-6}$ m^3/mol, the viscosity is only 1.6 times larger than in the case of zero activation volume.

In some simulations, we consider the thermal conductivity and coefficient of thermal expansion to be also dependent on temperature and pressure. Most of the existing models of Mercury's interior dynamics and evolution assume for these two quantities constant values, typically those representative for Earth's upper mantle, namely $k_r = 3$–4 W/(m K) and $\alpha_r = 2$–$3 \cdot 10^{-5}$ 1/K (e.g., Hauck et al., 2004; Grott et al., 2011; Tosi et al., 2013; Michel et al., 2013; Hauck et al., 2018; Guerrero et al., 2021). However, these values, are only attained across the relatively large pressure range of the Earth's upper mantle (up to ~24 GPa). The pressure at the base of Mercury's mantle does not exceed ~5.5 GPa (e.g., Hauck et al., 2013). At these pressures, it is the temperature dependence of k and α that controls to first order their value rather than the pressure dependence (Xu et al., 2004; Tosi et al., 2013b; Zhang et al., 2019). We assume a Mg-rich olivine composition and use a parametrization of the temperature and pressure dependence of k based on experimental data of Xu et al. (2004) for $(Mg_{0.9}Fe_{0.1})_2SiO_4$:

$$k(T,P) = (k_0 + k_1 P)\left(\frac{298}{T}\right)^{n_k}, \quad (11)$$

where k_0, k_1 and n_k are numerical coefficients (see Table 1) and P is the hydrostatic pressure. For the thermal expansivity, we use a parametrization based on ab-initio simulations of Li et al. (2007) for Mg_2SiO_4-forsterite:

$$\alpha(T,P) = (\alpha_0 + \alpha_1 T + \alpha_2 T^{-2}) \exp(-\alpha_3 P), \quad (12)$$

where α_0, α_1, α_2, and α_3 are again numerical coefficients (Table 1).

Fig. 2 shows profiles of viscosity, thermal conductivity and thermal expansivity calculated from Eqs. (10)–(12) along a hot (red) and a cold (blue) temperature profile (Fig. 2a). The viscosity profiles in Fig. 2b are calculated assuming a reference value of 10^{21} Pa s and an activation energy of 300 kJ/mol. The thermal conductivity in the convecting part of the mantle does not exceed 2 W/(m K) (Fig. 2c), much lower than the value commonly used in Mercury's simulations. For comparison, dashed lines in Fig. 2c also show thermal conductivity profiles for pure Mg-forsterite by Zhang et al. (2019) (dashed lines). As we will see in Section 4.3, already when using the parametrization of Eq. (11), the influence of a low thermal conductivity is large. Employing the even lower conductivities of Zhang et al. (2019) would render these effects even more pronounced. By using a slightly higher conductivity profile we qualitatively account for the fact Mercury's mantle also contains clino- and othopyroxenes whose thermal conductivity is higher than that of olivine (e.g., Wang et al., 2014; Guo et al., 2024). For simplicity, we also do not consider any dependence of the thermal conductivity and expansivity on composition. In other words, we do not change these two quantities in the newly produced crust by assigning them values characteristic, for example, of basalt. Basalitc rocks tend to have conductivities of about 2.5 W/(m K) at near surface conditions (e.g., Halbert and Parnell, 2022), slightly lower than the values calculated with Eq. (11). While this lower conductivity would enhance the insulating effects that we will discuss in Section 4.3, we do not expect it to qualitatively influence our conclusions.

Finally, the thermal expansivity is systematically higher than $4 \cdot 10^{-5}$ 1/K (Fig. 2d), up to twice the value that is often assumed, but, as we will show, the influence of α is not particularly large.

2.4. Radius change

Lobate scarps and wrinkled ridges, the compressive structures that prominently characterize Mercury's surface, are attributed to the global radial contraction of the planet (Byrne et al., 2014; Watters, 2021), which started early (e.g., Giacomini et al., 2015) and likely continued until present (Man et al., 2023), although possibly at a decreasing rate (Crane and Klimczak, 2017). We also compute the global and local radius change (ΔR) from our simulations as a post-processing step to assess the implications of different surface temperature distributions on this quantity. We compute ΔR as follows (Grott et al., 2011; Tosi et al., 2013; Hauck et al., 2018; Peterson et al., 2021):

$$\begin{aligned}\Delta R(t) &= \Delta R_c(t) + \Delta R_m(t) + \Delta R_{cr}(t) \\ &= \frac{R_c^3}{3R_p^2}\alpha_c\left(T_c(t) - T_{c,0}\right) + \frac{1}{R_p^2}\int_{R_c}^{R_p} \alpha_m\left(T_m(r,t) - T_{m,0}(r)\right) r^2 dr \\ &\quad + \frac{1}{f}\frac{\delta V}{V} D_{cr}(t), \end{aligned} \quad (13)$$

where ΔR_c and ΔR_m account for the contribution due to thermal expansion and contraction of the core and mantle, respectively, and ΔR_{cr} for the contribution due to mantle differentiation upon crust production. In the second line of the equation, R_c and R_p are the core and planet radius, respectively, α_c is the thermal expansivity of the core, $T_c(t)$ is the time-dependent core temperature calculated with Eq. (7) and $T_{c,0}$ its initial value, α_m is the thermal expansivity of the mantle, $T_m(r,t)$ is the laterally-averaged, time-dependent temperature profile and $T_{m,0}(r)$ its initial value, f and $\delta V/V$ are the fraction of extractable crustal components and the volume change upon melting (Kirk and Stevenson, 1989), and $D_{cr}(t)$ the time-dependent crustal thickness.

The values of f and of $\delta V/V$ are highly uncertain, and therefore, so is the expansion due to crust production. They depend on the unknown mantle composition and on the ratio of extrusive to intrusive volcanism, with $\delta V/V$ that could be anywhere between 0 and a few percent (Grott et al., 2011). While in principle they should be varied (Grott et al., 2011; Tosi et al., 2013), for simplicity we keep them fixed at $f = 0.4$ and $\delta V/V = 0.01$, which yield a relatively small positive contribution to the radius change due to crust production. However, since Mercury's surface record starts at ~4 Ga and a large part of the crust is produced before this time, the actual contribution of the term ΔR_{cr} for the observed radius change is minor compared to that of core and mantle cooling (see Sections 2.5 and 5.2).

2.5. Spin–orbit resonances and surface temperature distribution

We follow the approach of Vasavada et al. (1999), which we previously applied in Tosi et al. (2015), to calculate the mean distribution of the surface temperature not only for the present-day 3:2 spin–orbit resonance, but also for the hypothetical cases of synchronous rotation and 2:1 resonance (Figs. 3 and A.1). These distributions are obtained by averaging the temperature over one insolation cycle (2 years for 3:2, or 1 year for 1:1 and 2:1 resonances). We assume zero obliquity, fix the orbital eccentricity to 0.2, and calculate the thermal response of shallow surface and subsurface layers to solar and infrared radiation in dependence of various material properties: albedo, infrared emissivity, density, thermal conductivity, and heat capacity. All but the last two properties are fixed in time and representative of the present-day. The heat capacity and the thermal conductivity are considered temperature-dependent and, therefore, vary during the insolation cycle. Their temperature dependence mimics the thermophysical properties of lunar samples (Ledlow et al., 1992; Mitchell and de Pater, 1994; Vasavada et al., 1999). The model setup is identical to model TWO of Vasavada et al. (1999), which consists of two-layers: a 2-cm-thick top insulating layer and a more conductive and dense lower layer with a thickness of 78 cm. We use as surface temperature boundary condition for our simulations the temperature predicted by this model at a depth of 80 cm, where the influence of temperature changes along the orbit due to the skin effect is negligible.

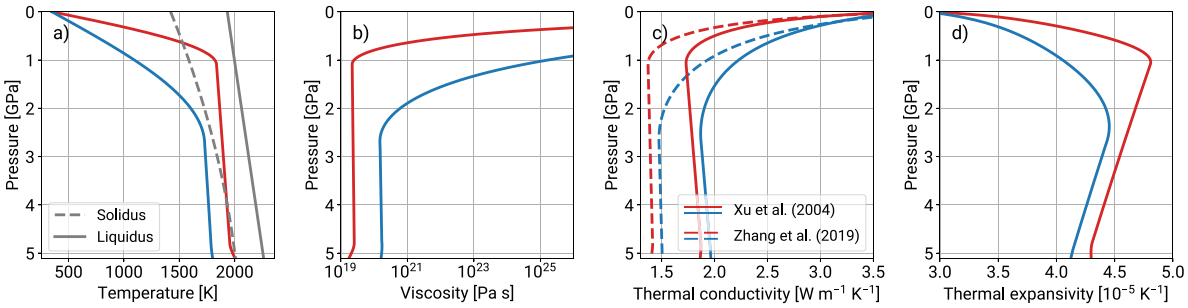

Fig. 2. Hot (red) and cold (blue) temperature profiles (a) and corresponding distributions of viscosity (b), thermal conductivity (c) and thermal expansivity (d) calculated according to Eqs. (10), (11) and (12), respectively. Gray lines in panel a denote the CMAS solidus and liquidus proposed by Namur et al. (2016). Viscosity profiles in panel b are calculated assuming $\eta_r = 10^{21}$ Pa s. (For interpretation of the references to color in this figure legend, the reader is referred to the web version of this article.)

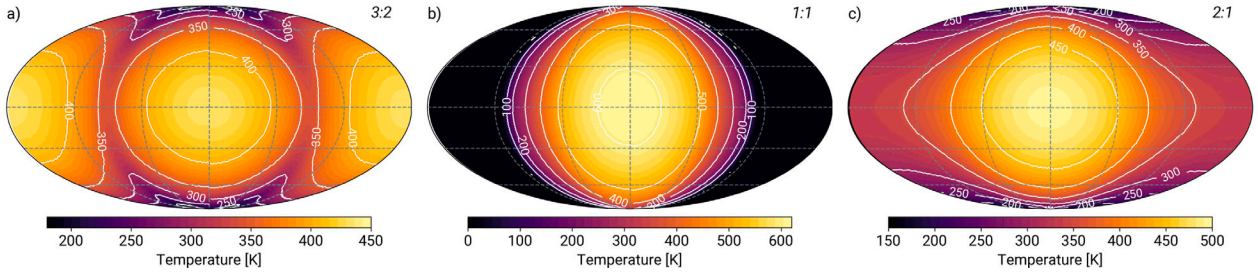

Fig. 3. Time-averaged surface temperature distribution in the case of (a) 3:2, (b) 1:1, and (c) 2:1 spin–orbit resonances for an assumed eccentricity of 0.2.

3. Model parameters and initial conditions

We carried out 30 simulations, which are listed in Table 2 along with their model parameters.

We focus on the role of the surface temperature distribution and compare simulations using a uniform temperature of 350 K, corresponding to the spatial average of the present-day temperature, and three different laterally-variable distributions corresponding to the present-day 3:2 resonance (Fig. 3a), and to either synchronous (Fig. 3b) or 2:1 (Fig. 3c) resonance, all calculated assuming an eccentricity of 0.2 (Section 2.5).

We vary the reference viscosity η_r between $5 \cdot 10^{20}$ and $5 \cdot 10^{21}$ Pa s. Values lower than $5 \cdot 10^{20}$ Pa s lead in some cases to numerical instabilities, while values higher than $5 \cdot 10^{21}$ Pa s cause the mantle to quickly become conductive, with little to no crust production. Although limited, this viscosity range is sufficient to disclose the influence of this parameter on the production of crust and radius change. We keep the activation energy and activation volume constant and set them to standard diffusion creep values for olivine $E^* = 300$ kJ/mol and $V^* = 6$ cm^3/mol (e.g., Karato and Wu, 1993). The contribution of non-linear dislocation creep could be important for Mercury, particularly in controlling the lifetime of convection (Jain and Solomatov, 2024). However, the importance of dislocation over diffusion creep depends crucially on the unknown grain size (e.g., Schulz et al., 2020; Jain and Solomatov, 2024) and, for simplicity, it is here neglected.

We consider two sets of simulations either with constant or with pressure- and temperature-dependent thermal conductivity and expansivity (Section 2.3). In the first case, we set $k = 3$ W/(m K) and $\alpha = 3 \cdot 10^{-5}$ 1/K as traditionally done in simulations of Mercury's evolution (e.g., Hauck et al., 2004; Grott et al., 2011; Tosi et al., 2013; Michel et al., 2013; Hauck et al., 2018; Guerrero et al., 2021). In the second case, we calculate the two parameters according to Eqs. (11) and (12).

We consider three different models for the initial abundance of the long-lived heat producing elements (HPE) U, Th, and K: one based on standard carbonaceous (CI) chondrites (McDonough and Sun, 1995); a second one based on enstatite (EH) chondrites (Wasson and Kallemeyn, 1988), and a third one (EH, low K) based on enstatite chondrites depleted in the moderately volatile K (Pirotte et al., 2023) (Fig. 4). On the one hand, the high abundance of K (800 ppm) in EH-chondrites, which are thought to be well representative of Mercury's bulk material (e.g., Ebel and Alexander, 2011; Nittler et al., 2011; Weider et al., 2012; Namur et al., 2016), renders their initial heat production rate of about 30% higher than that of CI-chondrites (40.7 pW/kg vs. 28.7 pW/kg). On the other hand, the initial heat production of K-depleted EH-chondrites (10.6 pW/kg) is only 26% of that of undepleted EH-chondrites. We neglect heating due to tidal dissipation as it is expected to be only a small fraction of the internal heating rate (Rivoldini et al., 2010).

In all simulations we enrich the crust (and correspondingly deplete the mantle) in HPE according to a constant factor chosen in such a way that the heat production of the crust matches the heat production obtained from the surface concentration of HPE as measured by MESSENGER (Peplowski et al., 2012) (gray line in Fig. 4).

We use the CMAS solidus and liquidus proposed by Namur et al. (2016) (gray lines in Fig. 2a), which were also employed by Padovan et al. (2017) to study mantle melting in response to basin-forming impacts. In all simulations, we set the initial CMB temperature to 2000 K, corresponding approximately to the solidus at the CMB.

Table 2
List of all simulated cases according to the following parameters: core radius (R_c), surface temperature distribution (T_s), reference viscosity (η_r), model of heat producing elements (HPE), use of heat piping, thermal conductivity (k), and thermal expansivity (α).

Simulation n.	R_c (km)	T_s	η_r (Pa s)	HPE	Heat piping	k	α
1	2015	Constant	10^{21}	EH (low K)	No	Constant	Constant
2	2015	3:2	10^{21}	EH (low K)	No	Constant	Constant
3	1955	3:2	10^{21}	EH (low K)	No	Constant	Constant
4	2015	3:2	$5 \cdot 10^{20}$	EH (low K)	No	Constant	Constant
5	2015	3:2	$5 \cdot 10^{21}$	EH (low K)	No	Constant	Constant
6	2015	3:2	10^{21}	EH (low K)	Yes	Constant	Constant
7	2015	3:2	10^{21}	EH (low K)	No	Variable	Variable
8	2015	3:2	10^{21}	EH (low K)	Yes	Variable	Variable
9	2015	1:1	10^{21}	EH (low K)	No	Constant	Constant
10	1955	1:1	10^{21}	EH (low K)	No	Constant	Constant
11	2015	1:1	10^{21}	EH (low K)	Yes	Constant	Constant
12	2015	Constant	10^{21}	CI	No	Constant	Constant
13	2015	3:2	10^{21}	CI	No	Constant	Constant
14	1955	3:2	10^{21}	CI	No	Constant	Constant
15	2015	3:2	$5 \cdot 10^{20}$	CI	No	Constant	Constant
16	2015	3:2	$5 \cdot 10^{21}$	CI	No	Constant	Constant
17	2015	3:2	$5 \cdot 10^{21}$	CI	Yes	Constant	Constant
18	2015	3:2	$5 \cdot 10^{21}$	CI	No	Constant	Variable
19	2015	3:2	$5 \cdot 10^{21}$	CI	No	Variable	Constant
20	2015	3:2	$5 \cdot 10^{21}$	CI	No	Variable	Variable
21	2015	3:2	$5 \cdot 10^{21}$	CI	Yes	Variable	Variable
22	2015	1:1	10^{21}	CI	No	Constant	Constant
23	1955	1:1	10^{21}	CI	No	Constant	Constant
24	2015	2:1	10^{21}	CI	No	Constant	Constant
25	2015	Constant	10^{21}	EH	No	Constant	Constant
26	2015	3:2	10^{21}	EH	No	Constant	Constant
27	2015	3:2	10^{21}	EH	Yes	Constant	Constant
28	1955	3:2	10^{21}	EH	Yes	Constant	Constant
29	2015	1:1	10^{21}	EH	No	Constant	Constant
30	2015	1:1	10^{21}	EH	Yes	Constant	Constant

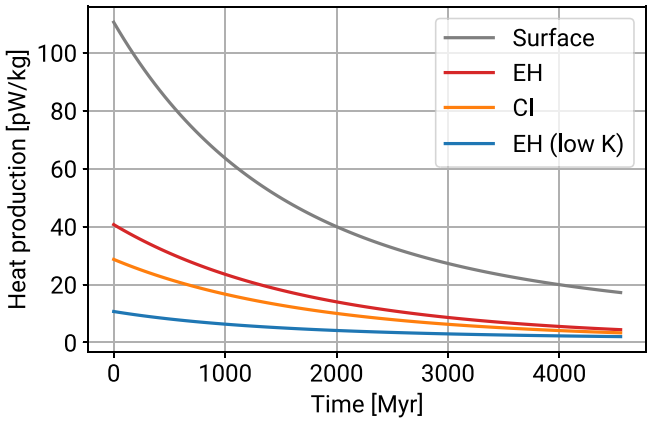

Fig. 4. Heat production due to U, Th and K based on their surface abundance as measured by MESSENGER (Peplowski et al. (2012), gray line) and on different bulk mantle abundances, namely enstatite chondrites (red line), CI chondrites (orange line), and enstatite chondrites depleted in K (blue line). (For interpretation of the references to color in this figure legend, the reader is referred to the web version of this article.)

For the mantle thickness (D), we test two values of 425 km and 485 km. According to recent interior structure models of Goossens et al. (2022), the two currently available estimates of the moment of inertia (0.349 ± 0.014 according to Mazarico et al. (2014) and 0.333 ± 0.005 according to Genova et al. (2019)) lead to distinct distributions of the radius of the outer core centered at 2015 km and 1955 km, respectively, thus implying a 60 km difference in the corresponding mantle thicknesses.

We initialize all simulations with a radial temperature distribution consisting of an upper thermal boundary layer of 50 km thickness that continues with a temperature profile that follows the solidus down to the CMB, whose initial temperature is 2000 K. Because of the gentle slope of the solidus near the CMB, this choice implies that no bottom thermal boundary is present at the beginning of the simulations. We do not vary the initial temperature distribution, but we note that choosing a cooler mantle temperature would imply, on the one hand, the presence of a bottom thermal boundary layer. This would accelerate the onset of convection and plume formation, promoting melting and crust production. On the other hand, a cooler mantle would initially cause a reduced crust production and it would tend to heat up with time due to internal heating. Therefore, qualitatively, we can expect the net effect to be similar to that of a hot mantle without a bottom thermal boundary layer.

In all simulations, we use a structured, projected grid with $1.72 \cdot 10^6$ and $1.96 \cdot 10^6$ grid cells for model cases using a mantle thickness of 425 km and 485 km, respectively. The grid has a uniform radial resolution of 10.5 km. Each radial shell is divided into the same number of cells (40962), resulting in a resolution at the CMB of 35.3 km for $D = 425$ km and 34.2 km for $D = 485$ km, and at the surface of 42.7 km. To track the mantle composition, we use 200 particles per cell.

4. Results

4.1. Surface temperature variations

We begin showing in Fig. 5 the influence of different surface temperature distributions on the convection planform and on the resulting crustal thickness after 100 Myr and 1000 Myr for three simulations assuming a mantle thickness of 425 km and HPE with CI abundance (simulations 12, 13 and 22 in Table 2). As illustrated by the distribution of temperature anomalies in the upper mantle below the stagnant lid (Fig. 5a–c and g–i), the convection planform in Mercury's thin silicate shell is always small-scale, independent of the surface temperature. Once up- and downwelling instabilities (red and blue structures, respectively) grow from the initial random perturbation prescribed on the temperature field, they remain anchored in their original position until the end of the simulations (1 Gyr) and likely longer due to secular cooling that will increase the mantle viscosity and reduce convective vigor.

The distribution of surface temperature imposes a clear long-wavelength pattern at depth. Although such a thermal perturbation does not affect the spatial scale of convection, it controls the location of anomalously hot and cold regions. When the present-day 3:2 temperature distribution is assumed (Fig. 5b and h), hot upwellings are concentrated beneath the two surface hot poles (Fig. 3a), while cold downwellings form preferentially at intermediate longitudes and at the cold poles. This effect becomes more striking when the surface temperature distribution associated with a synchronous rotation is assumed (Fig. 5c and i). In this case, the distribution of temperature anomalies becomes hemispherical with hot upwellings largely concentrated on the day-side and downwellings on the night-side. We observe a similar, yet less extreme, planform when using the surface temperature distribution associated with the 2:1 resonance (Fig. 3c), with temperature anomalies and corresponding crustal thickness shown in the Appendix in Fig. A.2.

Under the assumption of vertical melt extraction, the distribution of crust closely reflects the convection planform (Fig. 5d–f and j–l). While the crust can grow to a thickness in excess of 100 km and more after 1 Gyr of evolution above hot upwellings, nearly no crust is produced above regions where cold downwellings are located. This peculiar pattern is a direct consequence of the long-term stability of convection structures caused by the lack of significant lateral flow. While the 3:2 surface temperature distribution causes negligible large-scale lateral variations of the crustal thickness (Fig. 5e and k), when the 1:1 surface temperature distribution is assumed, the crust grows significantly thicker on the dayside than on the nightside, although several hundred million years are needed for such a difference to become substantial (compare Fig. 5f after 100 Myr and Fig. 5l after 1000 Myr).

We can gain further insight into the modeled crustal thicknesses by inspecting their spectra. We used the software pySHTools (Wieczorek and Meschede, 2018; Wieczorek et al., 2022) to perform a spherical harmonic analysis of the crustal thickness fields and to compute the corresponding power spectra. Fig. 6 shows such spectra up to spherical harmonic degree 20 for the three cases shown in Fig. 5 with the addition of another one based on a 2:1 surface temperature distribution (solid lines), as well as power spectra for the three crustal thickness models of Beuthe et al. (2020) presented in Fig. 1 (dashed lines). Spectra of our modeled crustal thicknesses are clearly different from those inferred from gravity and topography data. At relatively high degrees, approximately above degree 12, the power of the modeled spectra is systematically higher than that of the "observed" ones. This is due to the small-scale nature of our crust distribution, which closely reflects the convection planform because of the assumption of vertical melt extraction. By contrast, at lower degrees, the modeled spectra systematically underestimate those of the models of Beuthe et al. (2020). Nevertheless, models V0 and V4 by Beuthe et al. (2020) are characterized by a prominent degree-1 contribution due to the thick crust beneath the high-Mg region (red and blue dashed lines in Fig. 6). As expected, a strong degree-1 signal is obtained in our models when imposing 1:1 and, to a lesser extent, 2:1 surface temperature distributions (red and blue solid lines in Fig. 6). As already shown in Fig. 1, the U0 model of Beuthe et al. (2020) differs remarkably from V0 and V4. Similar to other models based on a uniform crustal density (e.g., Genova et al., 2019), it is characterized by relative maxima near the equator at 0 degree longitude and east of it, which exhibit some correlation with the hot poles of the 3:2 surface temperature pattern. This leads to a more prominent degree-2 signal (black dashed line in Fig. 6), which is at least qualitatively reproduced by our model based on the 3:2 surface temperature distribution (orange solid line in Fig. 6).

Fig. 7 shows the evolution of the globally-averaged CMB temperature and of the volume-averaged sub-lid mantle temperature (Fig. 7a), of the crust thickness (Fig. 7b), of the lid thickness (Fig. 7c), of the mantle depletion (Fig. 7d), of the radius change (Fig. 7e), and of the surface and CMB heat fluxes (Fig. 7f) for the same simulations shown in Fig. 5, including additionally the 2:1 resonance case. Apart from minor differences, the curves are barely distinguishable, indicating that, from a global perspective, the influence of different surface temperatures is essentially negligible. These results are qualitatively similar to those of previous 1D models (e.g., Tosi et al., 2013) showing evolutions characterized by an early phase of slight mantle heating (solid lines in Fig. 7a) and by a rapid crust production during the first few hundred million years that results in an average crust thickness of ∼40 km, well compatible with predictions from gravity and topography data.

In Fig. 7e, for the case with constant surface temperature (gray lines), we additionally show how the total radius change (solid gray line) consists of the contributions due to core cooling (dashed gray line), mantle cooling (dashed-dotted gray line), and crust production (dotted gray line). As previously shown by Grott et al. (2011) and Tosi et al. (2013), the latter tends to slightly offset the total global contraction, which, in these simulations, is substantial: ∼4 km during the first Gyr of evolution.

Due to the choice of the initial temperature profile lying on the solidus, the CMB heat flux is only ∼1 mW/m^2 at the beginning of the evolution (dashed lines in Fig. 7f). It increases rapidly to ∼10 mW/m^2 because of mantle cooling associated with the onset of convection, but then decreases to settle at the constant value of about 4.5 mW/m^2 until the end of the simulation. Such a low heat flux would hardly be sufficient to generate an early magnetic field via thermal convection in the core, for which the minimum critical value is ∼12 mW/m^2 (e.g., Tosi and Padovan, 2021). Indeed detailed 1D models of the evolution of the core indicate that Mercury's dynamo is powered throughout the evolution by latent heat released upon solidification of an Fe-Si core (Knibbe and van Westrenen, 2018; Davies et al., 2024), whose parametrization should be incorporated also in future dynamic mantle models.

While the global evolution is hardly affected by the different surface temperature distributions, at a regional scale, the influence can be significant. In Fig. 8, we show the same quantities of Fig. 7, but averaged within an area delimited by a circle with a radius of 1500 km – approximately the size of the high-Mg region (Weider et al., 2015) – centered at the hottest (solid lines) and coldest pole (dashed lines) of the respective surface temperature distribution (see Fig. A.1 in the Appendix). For all three distributions shown in the figure, the hottest pole is at the equator and 180 ° longitude. For the 3:2 and 2:1 distributions, the coldest pole corresponds to one of the geographic poles, while for the 1:1 distribution it corresponds to the anti-solar point.

Similar to the global evolution of Fig. 7, a short initial phase of mantle cooling due to the onset of convection is followed by a temperature rise caused by the abundant radiogenic heating until about 200 Myr, after which monotonic cooling begins with a rate that is faster beneath the cold poles than beneath the hot poles (compare dashed and

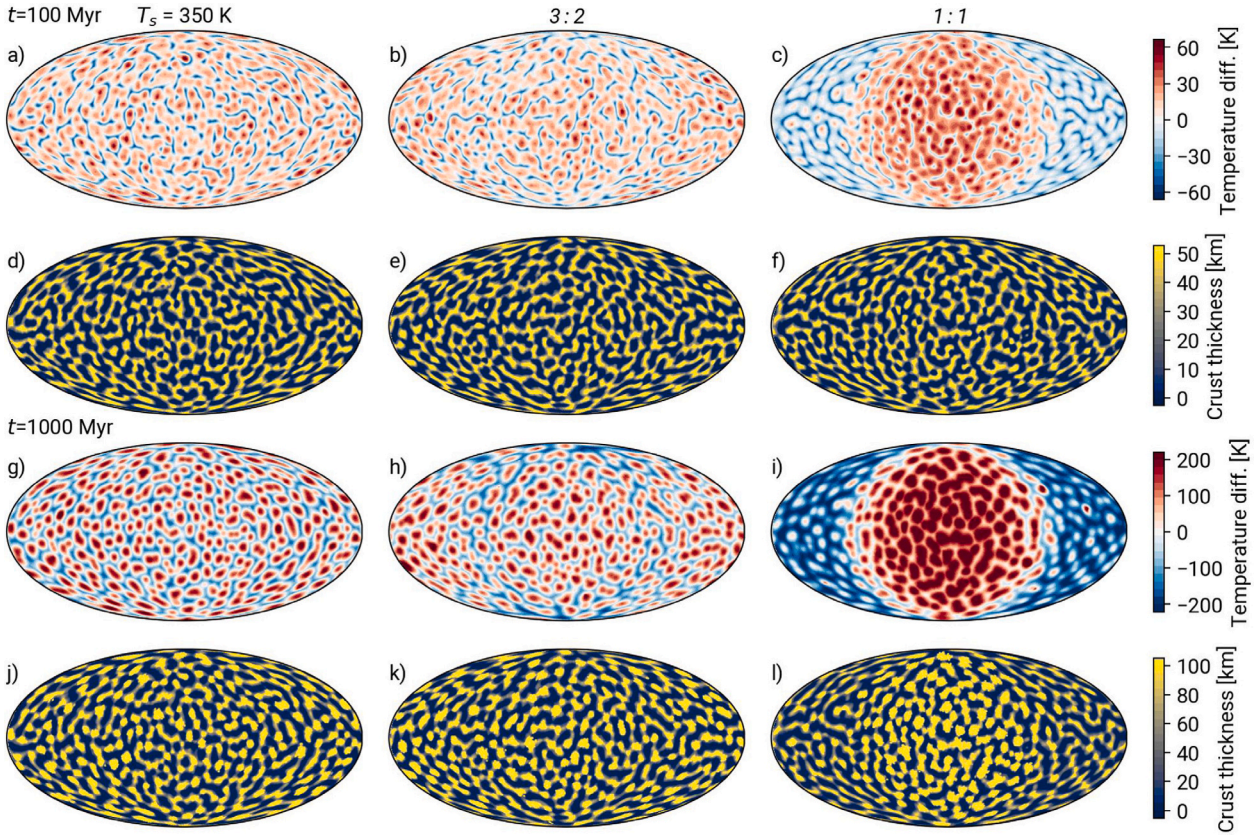

Fig. 5. Upper mantle temperature anomalies and crustal thickness after 100 Myr (a–f) and 1000 Myr (g–l) of evolution for simulations based on CI abundance of heat producing elements and using three distributions of surface temperature: constant at T_s = 350 K (left column, simulation 12), and variable according to the 3:2 pattern of Fig. 3a (central column, simulation 13), and according to the 1:1 pattern of Fig. 3b (right column, simulation 22). Results from simulation 24, which uses the 2:1 pattern of Fig. 3c do not present significant qualitative differences in terms of convection wavelength and influence of surface temperature with respect to those shown here, and are reported in the Appendix (Fig. A.2).

solid lines in Fig. 8a). Due to the high temperature of the hot poles, the stagnant lid remains significantly thinner than beneath the cold poles where it tends to grow faster (Fig. 8c). This effect is particularly evident in the case of the 1:1 resonance where the difference in the thickness of the lid beneath the two regions can reach nearly 70 km after 1 Gyr (compare red lines in Fig. 8c). Such a difference is much less prominent in the 2:1 case (blue lines) and even less in the 3:2 case where it is limited to ∼15 km at most (orange lines). The fact that beneath the cold poles the lid is thicker than beneath the hot poles is at the origin of the higher, volume-averaged sub-lid temperatures beneath the cold poles (compare dashed and solid lines in Fig. 8a). In fact, the sub-lithospheric mantle beneath the cold pole is nearly isothermal, while, due to the thinner lid, the mantle beneath the hot pole also includes part of the thermal boundary layer (see Fig. 9). As the latter occupies a relatively large volume, the volume-averaged sub-lid temperature is colder under the hot pole than under the cold pole.

As expected, partial melting occurs in regions where the mantle is hot and the stagnant lid thin. Indeed, in the case of the 1:1 resonance, the average thickness of the crust beneath the hot and cold poles reaches 45 km and 32 km, respectively (solid and dashed red lines in Fig. 8b). However, it takes at least ∼200 Myr for such differences to develop significantly. As pointed out above upon discussing Fig. 5, lateral differences in crustal thickness are minor when considering the surface temperature distribution associated with the other two resonances, 3:2 and 2:1. In the first case, the maximum difference in the thickness of the crust between the hot and cold poles is about 2.5 km, in the second only 4 km (orange and blue lines in Fig. 8b). As expected, the evolution of the mantle depletion (Fig. 8d) closely mirrors the evolution of the crust.

The more rapid lid growth and reduced crust production beneath the cold poles lead to a higher rate of radial contraction than beneath the hot poles (compare solid and dashed lines in Fig. 8e). Again, this effect is most evident in the 1:1 case, where the difference in the average radial contraction beneath the two poles reaches 3.1 km after 1 Gyr (red lines) compared to 1 km in the 2:1 case (blue lines), and only 0.6 km in the 3:2 case (orange lines).

On the one hand, the differences in the surface heat fluxes between hot and cold poles are initially significant – particularly in the 1:1 case because of the largest surface temperature difference – and tend to diminish during the evolution (upper lines in Fig. 8f). On the other hand, the differences in CMB heat fluxes are negligible (lower lines in Fig. 8f) because, even after 1 Gyr, the surface temperature pattern has reached the mantle but not yet the CMB (see also Fig. 9e). Therefore, during this phase of the evolution, lateral differences in the CMB heat flux, which in principle could affect dynamo generation, are not expected.

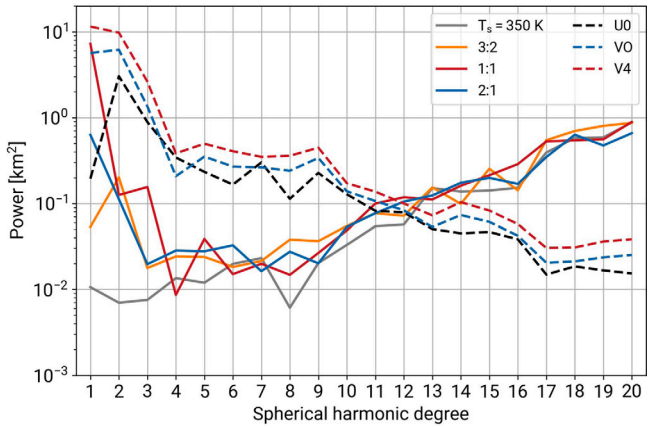

Fig. 6. Power spectra of the crustal thickness distribution as a function of spherical harmonic degree for four of our simulations (12, 13, 22 and 24) with different surface temperature distributions (solid lines), and for the three crustal thickness models U0, V0 and V4 by Beuthe et al. (2020) derived from gravity and topography data (dashed lines). (For interpretation of the references to color in this figure legend, the reader is referred to the web version of this article.)

Considering a thicker mantle (485 km instead of 425 km) has a relatively small influence on the interior evolution, independent of the choice of the surface temperature distribution (see Fig. A.3 in the Appendix). Therefore, in the rest of the paper, we will limit our detailed discussion to simulations considering a mantle thickness of 425 km.

Radial profiles of a few key quantities provide further insight into the different evolution of the mantle beneath the hot and cold surface regions. For the 3:2 and 1:1 cases, Fig. 9 shows radial profiles of temperature (Fig. 9a and e), viscosity (Fig. 9b and f), root mean square velocity (Fig. 9c and g), and mantle depletion (Fig. 9d and h), after 100 Myr (top line) and 1000 Myr (bottom line) as in Fig. 5. The solid and dashed lines correspond to profiles calculated beneath the hot and cold poles. These are obtained by laterally averaging the respective quantities over the mantle volume underlying the circles with radii of 1500 km centered at the hot and cold poles and discussed above in the context of the timeseries (see also Fig. A.1 in the Appendix). Profiles for the constant surface temperature and 2:1 cases are not shown here for better visibility, but are qualitatively similar and plot between the two cases shown in the figure (see Fig. A.4 in the Appendix).

Initially, temperature and viscosity variations due to the different surface temperature distributions are largely confined to the stagnant lid (Fig. 9a and b), with the velocity and depletion profiles that do not exhibit significant differences below the hot and cold poles (Fig. 9c and d). After 1 Gyr, as previously recognized by Tosi et al. (2015), the surface temperature perturbation has reached deep in the convecting part of the mantle below the stagnant lid (Fig. 9e and f), which is approximately located at the depth where the velocity departs from zero (Fig. 9c and g). The 3:2 case causes a difference between the hot and cold profiles of ∼100 K near the base of the stagnant lid, which is quite significant but much smaller than the ∼400 K arising in the presence of the 1:1 surface temperature distribution, demonstrating that in this case the dayside and nightside would experience remarkably different evolutions.

These differences in mantle temperature lead in turn to viscosity profiles (Fig. 9f) that explain the widely different stagnant lid thicknesses shown in Fig. 8c, as well as the differences observed in the velocity and depletion profiles (Fig. 9g and h). The velocity profiles exhibit two maxima: one at the CMB, indicative of rising hot upwellings, and one in the mid mantle, representing the signature of sinking parts of the cold lithosphere (Fig. 9g).

As suggested by the depletion profiles (Fig. 9d and h), melting occurs throughout the convecting mantle also with two peaks, one above the CMB and a second, slightly more prominent, beneath the stagnant lid. Similar to the other profiles, no significant differences between the hot and cold regions are present after 100 Myr. Differences become evident after 1 Gyr. In the 1:1 case, the average depletion after 1 Gyr is 14.7% beneath the hot pole and 10.9% beneath the cold pole, while for the 3:2 case, these figures reduce to 13.2% and 12.5% confirming that the present-day resonance is likely not responsible for large-scale differences in mantle melting.

4.2. Internal heat production and mantle viscosity

For simulations using the present-day 3:2 surface temperature distribution, Fig. 10 shows how the global evolution of a few key quantities is influenced by different reference viscosities (left column, simulations 13, 15 and 16) and different HPE models (right column, simulations 2, 13 and 26).

Increasing (or decreasing) the viscosity with respect to the reference value of 10^{21} Pa s causes the mantle and core to cool slower (or faster) and the planet to contract less (or more). Although increasing the viscosity by a factor of 5, from 10^{21} to $5 \cdot 10^{21}$ Pa s, leads to a hotter mantle and core (blue lines in Fig. 10a), the accompanying final crustal thickness decreases from 39 to 26 km (orange and blue lines in Fig. 10e) as a consequence of the much thicker stagnant lid (Fig. 10c). By contrast, reducing the viscosity by a factor of 2, from 10^{21} to $5 \cdot 10^{20}$ Pa s, nearly doubles the final crustal thickness (orange and red lines in Fig. 10c).

The behavior upon varying the amount of HPE is more straightforward, with temperatures and crustal thickness that are positively correlated with HPE concentration (Fig. 10b, f), and lid thickness and radius change negatively correlated (Fig. 10d, h).

Although reducing (increasing) the reference viscosity and increasing (reducing) the amount of HPE have similar effects on the volume of crust produced, the two parameters act differently on the timing of crust production and on radius changes. For the three values of the reference viscosity, most of the crust is produced within 350 and 500 Myr (Fig. 10e). For low viscosities, the thinner lid facilitates melt production, but the mantle tends to be cooler. For high viscosities, the thicker lid tends to prevent melt production, while the mantle remains hotter. The trade-off between these two competing effects ultimately causes the bulk of the crust to be emplaced over a very similar time span, only weakly dependent on the reference viscosity.

By contrast, crust production is extremely short-lived when the HPE model with the lowest abundance is used, with 90% of the final crust thickness attained after ∼280 Myr and after ∼560 Myr when using the lowest and highest HPE abundances, respectively (compare blue and red lines in Fig. 10f). A high internal heat production causes both a thinner lid and a hotter mantle, ultimately resulting in extensive and prolonged melting and crust production.

Models with a high reference viscosity or a high HPE abundance result in the smallest radial contraction rates as a consequence of their tendency to retard mantle cooling. For example, after 1 Gyr, we obtain a radius change of ~ -2.5 km for the case with $\eta_r = 5 \cdot 10^{21}$ Pa s and the HPE-CI model (blue line in Fig. 10g), and of ~ -1.8 km for the case with $\eta_r = 10^{21}$ Pa s and the HPE-EH model (red line in Fig. 10h). Decreasing the reference viscosity, and in turn enhancing mantle cooling, slightly increases the contraction rate, but not in a straightforward way. The radius change after 1 Gyr is actually smaller for the lowest reference viscosity ($\eta_r = 5 \cdot 10^{20}$ Pa s) than for the intermediate one ($\eta_r = 10^{21}$ Pa s) as a consequence of the more pronounced crust production that tends to offset planetary contraction (compare solid orange and red lines in Fig. 10g). If the positive contribution to the radius change due to crust production is neglected and only the thermal contraction of core and

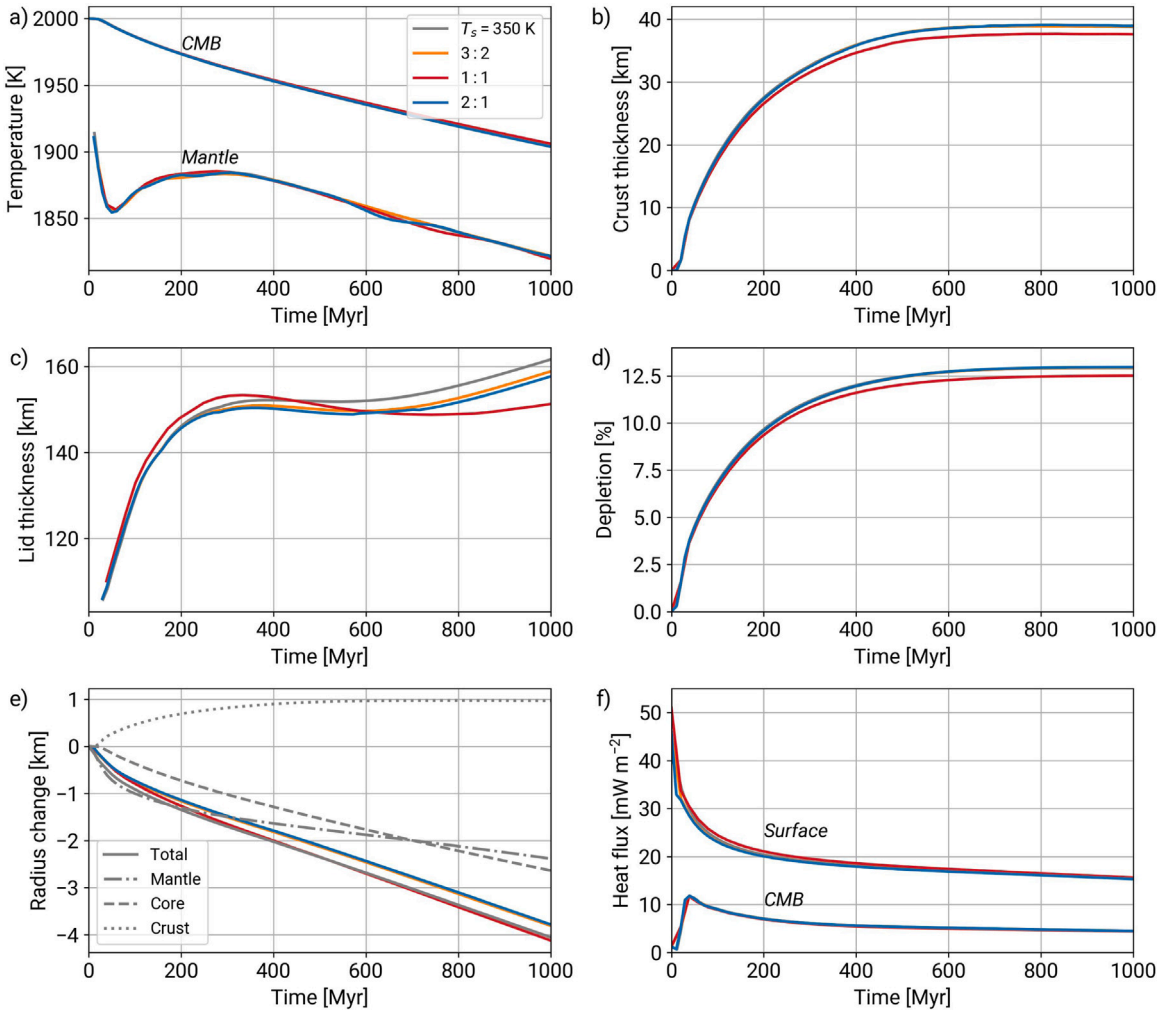

Fig. 7. Timeseries of (a) volume-averaged sub-lid temperature, (b) crustal thickness, (c) stagnant lid thickness, (d) depletion, (e) radius change, and (f) surface and CMB heat flux for the same simulations shown in Fig. 5 plus one corresponding to the 2:1 surface temperature distribution, which is shown in Fig. A.2. All quantities are global averages. (For interpretation of the references to color in this figure legend, the reader is referred to the web version of this article.)

mantle are considered, the influence of reference viscosity is clearly monotonic (dotted lines in Fig. 10g).

Decreasing the heat production rate has instead the very clear effect of causing rapid mantle and core cooling and a limited crust production. Indeed, in the case with the lowest HPE abundance, after 1 Gyr the radius change is as high as −6 km (blue line in Fig. 10h).

4.3. Thermal conductivity, thermal expansivity and heat-piping

In this section, we describe two factors that typically receive less attention in studies of planetary evolution, namely the influence of variable thermal conductivity and expansivity, and of the so-called heat piping effect.

As discussed in Section 2.3, over the pressure and temperature range of Mercury's mantle, the thermal conductivity of Mg-rich olivine is less than ∼2 W/(m K), significantly lower than the typical value of ∼3–4 W/(m K) assumed in interior studies of Mercury. Similarly, with values of $4–5 \cdot 10^{-5}$ 1/K, the thermal expansivity is higher than $\sim 3 \cdot 10^{-5}$ 1/K, which is often assumed. On the one hand, variations of thermal conductivity influence the heat transfer in the conductive crust and stagnant lid, with low values of k that will retard the cooling of the mantle. On the other hand, variations of the thermal expansivity influence mantle buoyancy and the strength of convection (see the right-hand-side of Eq. (2)), with high values of α that will increase the effective Rayleigh number of the system and facilitate mantle cooling.

The abundant partial melts migrating upward to form the crust can be easily extruded at the surface. The widespread volcanic plains covering Mercury's northern hemisphere, dated to ∼3.7 Ga (Denevi et al., 2013), indicate that melt extrusion persisted for hundred of millions of years after global-scale resurfacing at 4 Ga (Marchi et al., 2013). Extruded melts rapidly cool to space, solidify and become buried by subsequent eruptions. This process results in a net downward advection of cold material that can affect the temperature profile of the lithosphere and upper mantle (Moore and Webb, 2013; Peterson et al., 2021), and in turn melt and crust production, and radius change.

Since considering variable conductivity, variable expansivity, and heat piping results in competing effects, it is interesting to compare the influence of these factors on the evolution of the interior. Fig. 11 shows timeseries of globally-averaged quantities for six different models, all of which assume a CI abundance of HPE, a reference viscosity of $5 \cdot 10^{21}$

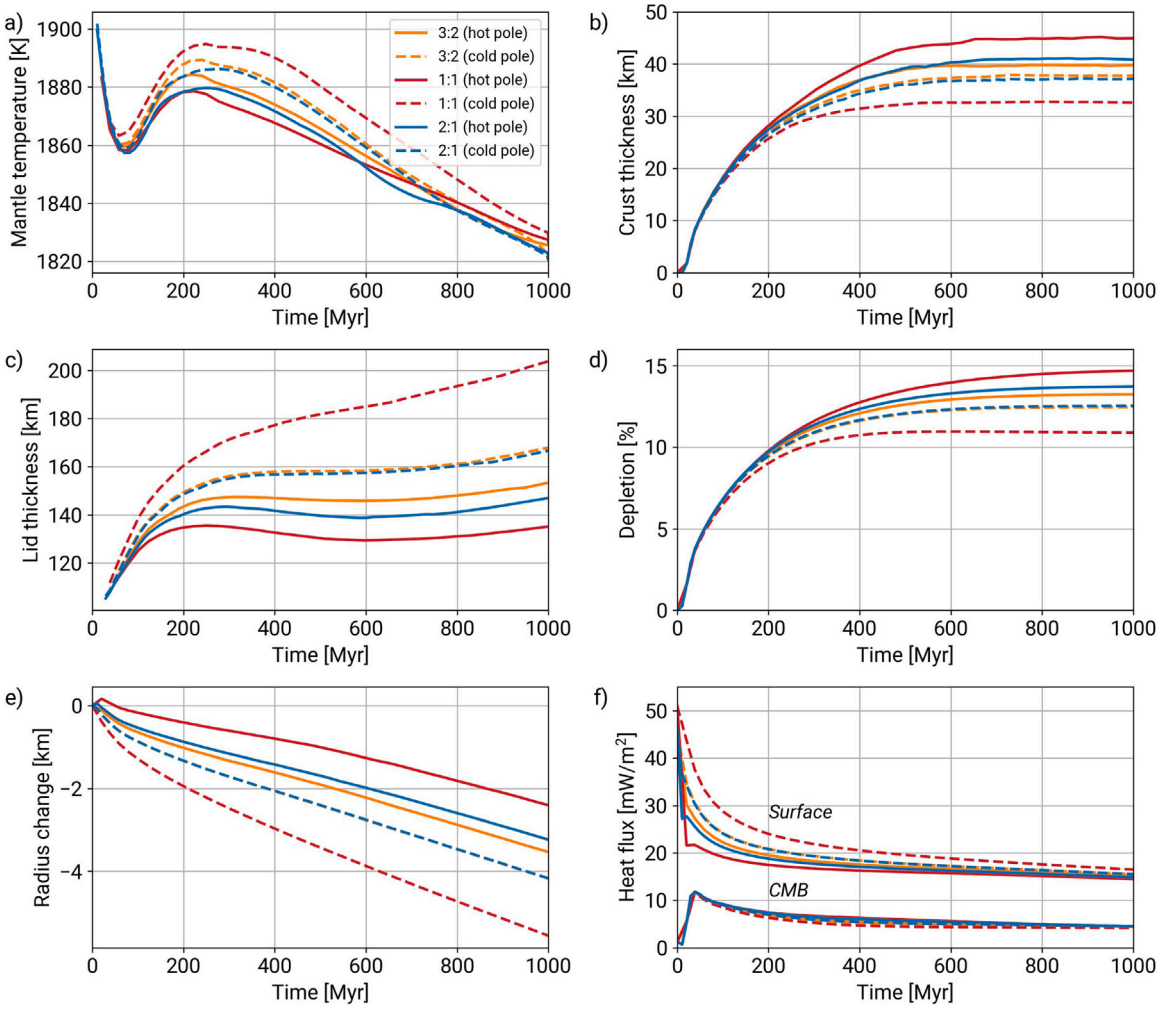

Fig. 8. Timeseries of (a) volume-averaged sub-lid temperature, (b) crustal thickness, (c) stagnant lid thickness, (d) depletion, (e) radius change, and (f) surface and CMB heat fluxes for the same simulations shown in Fig. 7 apart from the one with constant surface temperature. All quantities are averaged over a circle with a radius of 1500 km centered where the surface temperature is highest (hot pole, solid lines) or lowest (cold pole, dashed lines). See text for details and Fig. A.1. (For interpretation of the references to color in this figure legend, the reader is referred to the web version of this article.)

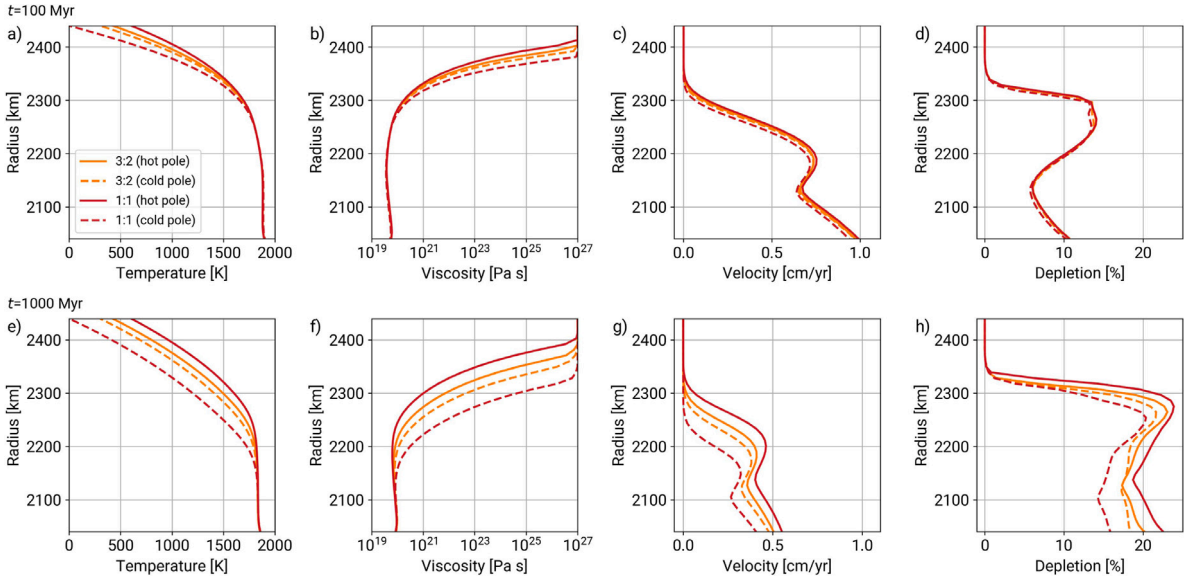

Fig. 9. Radial profiles of temperature (a, e), viscosity (b, f), flow velocity (c, g) and depletion (d, h) after 100 Myr (top line) and 1000 Myr (bottom line) for the 3:2 (orange lines) and 1:1 (red lines) cases (simulations 13 and 22, respectively). Solid and dashed lines refer to profiles beneath the hot and cold poles, respectively. (For interpretation of the references to color in this figure legend, the reader is referred to the web version of this article.)

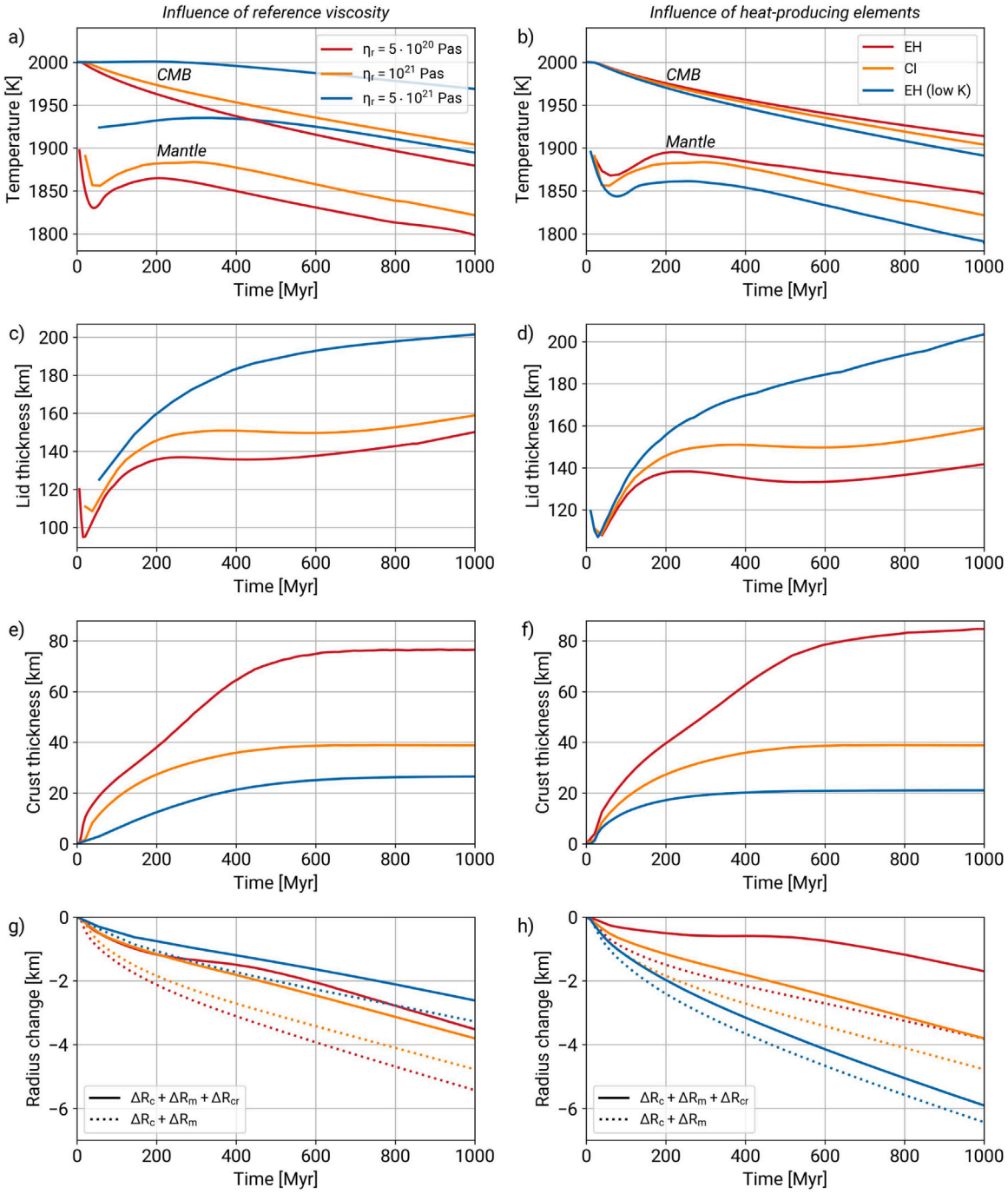

Fig. 10. Timeseries of (a, b) volume-averaged sub-lid temperature and CMB temperature, (c, d) lid thickness, (e, f) crustal thickness and (g, h) radius change for models with HPE-CI abundance and different reference viscosities (left column, simulations 13, 15 and 16), and models with a reference viscosity of 10^{21} Pa s and different HPE abundances (right column, simulations 2, 13 and 26). In panels g and h, the different line styles indicate contributions to radius change due to core, mantle and crust (solid lines) and due to core and mantle only (dotted lines). All models assume the present-day surface temperature distribution corresponding to the 3:2 pattern. All quantities are global averages. (For interpretation of the references to color in this figure legend, the reader is referred to the web version of this article.)

Pa s, and the present-day 3:2 surface temperature distribution. We can consider the solid blue line as reference case, which corresponds to a simulation with a constant thermal conductivity of 3 W/(m K), a constant thermal expansivity of $3 \cdot 10^{-5}$ 1/K, and no heat piping (simulation 16).

Including a variable thermal expansivity (simulation 18 and gray lines in the left panels of Fig. 11) causes a slightly faster cooling of mantle and core (Fig. 11a), thinning of the stagnant lid (Fig. 11c), a more rapid crust production with a final crustal thickness only about 3.5 km thicker than in the reference case (Fig. 11e), and a significantly higher rate of radius change due to the increased thermal contraction

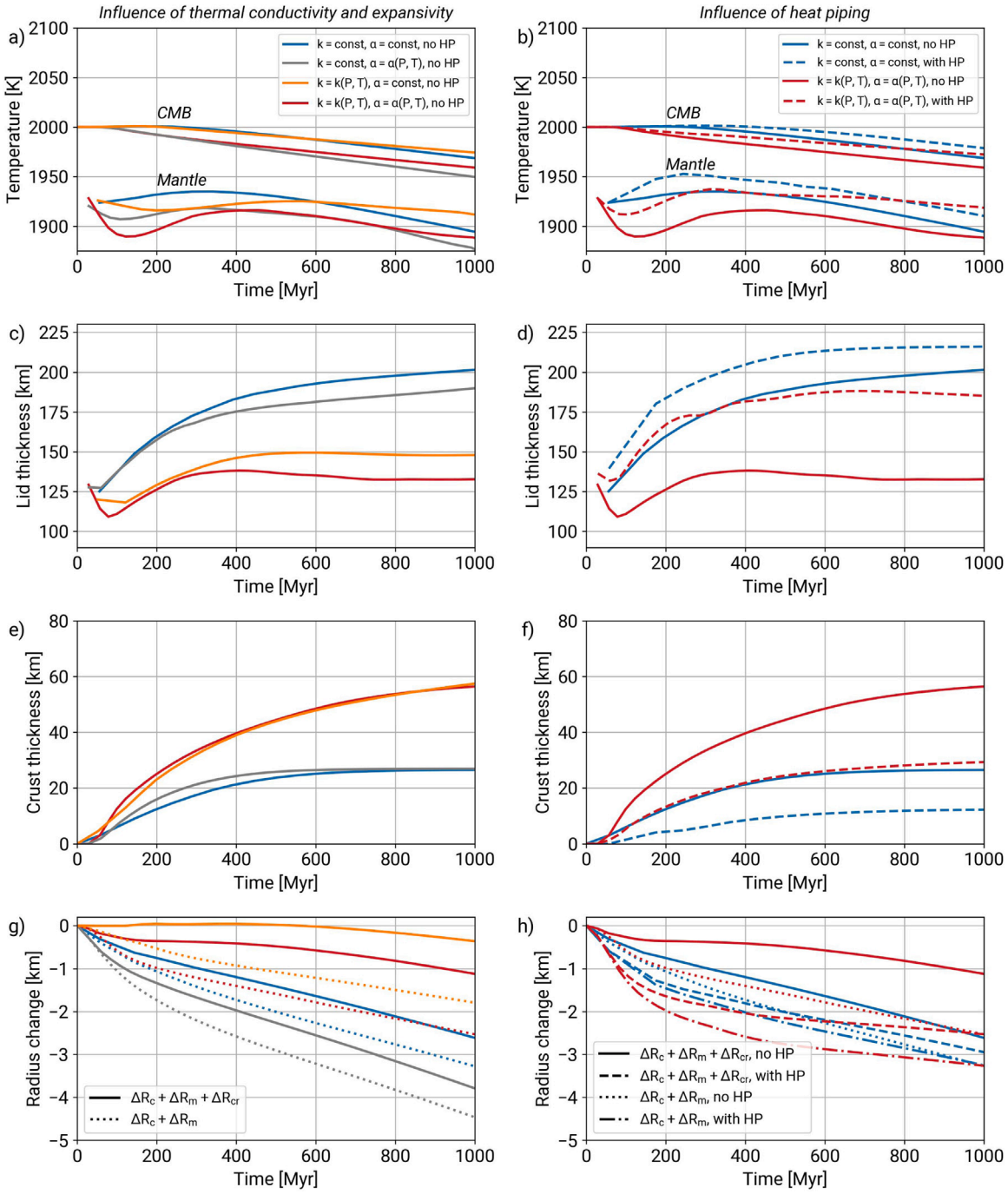

Fig. 11. Timeseries of (a, b) volume-averaged sub-lid and CMB temperatures, (c, d) lid thickness, (e, f) crustal thickness, and (g, h) radius change for models with HPE-CI abundance, a reference viscosity of $5 \cdot 10^{21}$ Pa s, and different combinations of constant and variable thermal conductivity and expansivity (left column and simulations 16, 18, 19 and 20), and presence or absence of the heat piping (HP) effect (right column and simulations 16, 17, 20 and 21). In panels g and h, the different line styles indicate contributions to radius change due to core, mantle and crust (solid lines in panel g and solid or dashed lines in panel h), and due to core and mantle only (dotted lines in panel g and dotted or dashed-dotted lines in panel h). All models assume the present-day surface temperature distribution corresponding to the 3:2 pattern. All quantities are global averages. (For interpretation of the references to color in this figure legend, the reader is referred to the web version of this article.)

of the mantle (Fig. 11g). A variable, hence comparatively low, thermal conductivity (simulation 19 and orange lines in Fig. 11) dramatically slows down mantle cooling with two major consequences. First, it causes intense and long-lived crust production. After 1 Gyr of evolution, the crust is more than twice as thick as in the reference case and is still growing (compare orange and blue lines in Fig. 11e). Second, it slows down radial contraction to the point that the net radius change is approximately zero for about 600 Myr when the expansion contribution

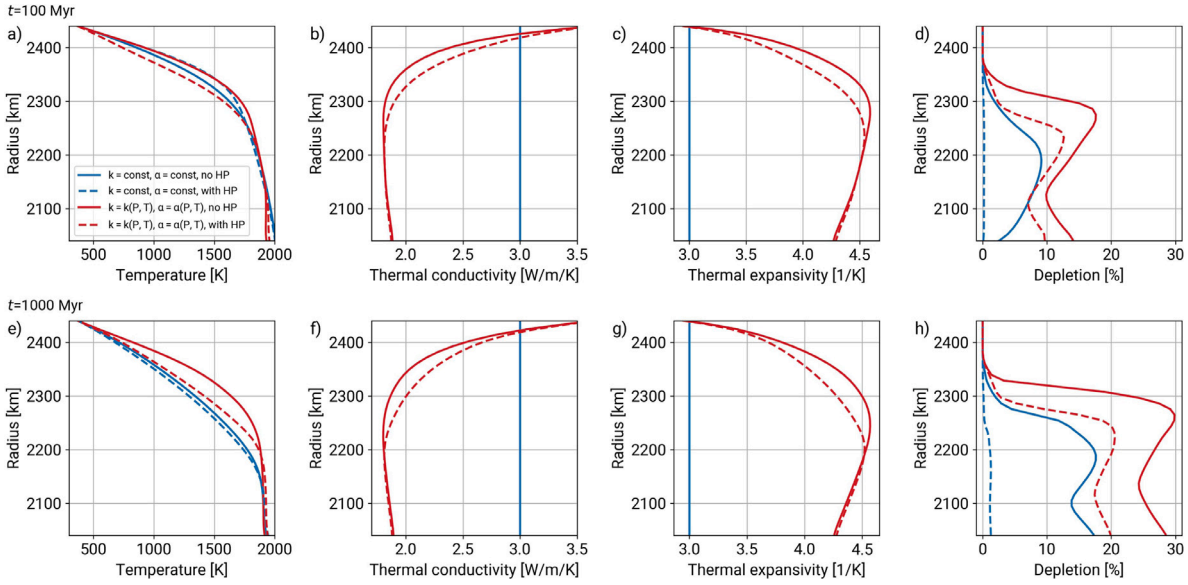

Fig. 12. Radial profiles of temperature (a, e), thermal conductivity (b, f), thermal expansivity (c, g), and depletion (d, h) after 100 Myr (top line) and 1000 Myr (bottom line) for the same cases shown in the right panels of Fig. 11 (i.e. simulations 16, 17, 20 and 21). (For interpretation of the references to color in this figure legend, the reader is referred to the web version of this article.)

due to crust production is taken into account (solid orange line in Fig. 11g). When both variable thermal conductivity and expansivity are considered (simulation 20 and red lines in Fig. 11), the evolution is similar to the case where only the thermal conductivity is variable (compare red and orange lines in Fig. 11), with slightly increased crust production and radius change induced by the higher thermal expansivity.

In terms of crust production, considering variable thermal expansivity and conductivity leads to evolutions that seem difficult to reconcile with Mercury's crustal record. The resulting crustal thickness exceeds ~60 km, corresponding to the upper end of the range inferred from gravity and topography data, and the time of crust production extends well beyond ~1 Gyr, considered to mark the end of widespread volcanism (see Section 1.1). Considering the influence of extrusive volcanism through the heat piping effect dramatically changes this picture. Dashed lines in the right panels of Fig. 11 correspond to models that include this effect (simulations 17 and 21). As illustrated in previous numerical models (Moore and Webb, 2013; Peterson et al., 2021), the downward advection of cold material causes thickening of the lithosphere (Fig. 11d) and in turn a much reduced crust production (Fig. 11f). When considering constant k and α, the crust thickness after 1 Gyr decreases from 26 km to 12 km (solid and dashed blue lines in Fig. 11f). With variable k and α, it decreases from 65 km to 33 km (solid and dashed red lines in Fig. 11f). The effect is also evident when looking at the radius change (Fig. 11h), which increases rapidly during the phase of lithosphere growth and continues at a decreased rate (compare solid and dotted lines, as well as dashed and dashed-dotted lines in Fig. 11h).

This behavior, as well as the effects due to variable k and α can also be recognized in the laterally averaged profiles at 100 and 1000 Myr shown in Fig. 12. Particularly evident are the role of variable conductivity and expansivity in shifting the thermal profiles to higher temperatures, thereby causing strong mantle melting and depletion (red lines in Fig. 12 and simulations 20 and 21), and of heat piping in reducing this effect (dashed lines in Fig. 12, simulations 17 and 21).

While the temperature distribution in the lithosphere and upper mantle is strongly influenced by heat piping, the effect on the CMB temperature is barely measurable (compare solid and dashed lines in Fig. 11b and a,e). Interestingly, when heat piping is considered, the CMB temperature is even slightly higher since the thicker stagnant lid tends to keep the deep mantle hotter. This behavior differs from what was reported by Peterson et al. (2021) who found that heat piping not only causes a higher rate of radius change, which we also observe (Fig. 11h), but also a stronger core cooling that could favor early dynamo generation. The discrepancy could be a consequence of the use by Peterson et al. (2021) of a 1D parameterized thermal model, where the evolution of the CMB temperature is tightly coupled to the evolution of the upper mantle temperature through an imposed (theoretical) adiabatic temperature gradient in the mantle.

5. Discussion

5.1. Evolution of the crust

Constructing dynamic models that can self-consistently reproduce the characteristics of the lateral distribution of Mercury's crustal thickness inferred from gravity and topography data (Fig. 1) remains challenging. Models derived from gravity and topography data and based on uniform crustal density (model U0 in Fig. 1a) have the highest crustal thickness near the equator that roughly correlates with the hot poles resulting from the present-day 3:2 surface temperature distribution (Fig. 3a). In model U0 of Beuthe et al. (2020), for example, the difference between the crustal thickness beneath the hot pole at 0 degrees longitude and the crustal thickness beneath the north pole is about 10 km (when averaged over a circular area with a radius of 1500 km), much larger than the mere 2.5 km obtained in our models (e.g., orange lines in Fig. 8b). The differences in surface temperature caused by the present spin–orbit resonance are simply not sufficiently large to induce significant lateral variations in crustal thickness.

A large-scale crustal thickness anomaly such as the one beneath the high-Mg region inferred by Beuthe et al. (2020) (models V0 and V4 in Fig. 1b and c) cannot be easily reproduced when considering a uniform surface temperature or the present-day surface temperature distribution. Based on the distribution of large basins and on

orbital dynamics simulations, low-order spin–orbit resonances such as synchronous rotation or 2:1 are considered more plausible than the present one during Mercury's early evolution, at times when the bulk of the crust was probably being formed (Correia and Laskar, 2012; Wieczorek et al., 2012; Knibbe and van Westrenen, 2017). We tested the hypothesis that the surface temperature variations that accompany these resonances could favor the formation of large-scale variations in crustal thickness by promoting mantle flow and melting of hot material beneath the surface hot spots. In the presence of a synchronous rotation, the temperature contrast between the day and night sides (Fig. 3b) is sufficiently large to induce beneath the day side the formation of a crust on average 12 km thicker than beneath the night side (red lines in Fig. 8b). Although the influence of the surface temperature is evident here, the discrepancy with respect to the crustal thickness models is still significant, and even more so upon considering a 2:1 resonance, which produces nearly negligible lateral variations in crustal thickness (blue lines in Fig. 8b). In the models V0 and V4 by Beuthe et al. (2020), for example, the average crustal thickness beneath the high-Mg region is ∼50 and 70 km, respectively 20 km and 25 km higher than the corresponding global mean crustal thickness.

In our models, the distribution of crust closely reflects the hemispherical temperature pattern, with the small-scale signal of mantle convection superimposed. The high-Mg region and the accompanying crustal anomaly do not appear to be hemispherical; instead, they are largely concentrated in the northern hemisphere. However, the resolution of MESSENGER data in the southern hemisphere is poor, so it cannot be ruled out that the high-Mg anomaly is actually more extensive, possibly extending further into the southern hemisphere. If that were the case, the crustal distribution predicted by our models would align more closely with that inferred from gravity and topography data. If not, large-scale compositional heterogeneities in the mantle – causing laterally-varying melting and crust production – could be responsible for the formation of the high-Mg region and its thicker crust (e.g., Namur et al., 2016; Wang et al., 2022). The physical mechanisms leading to such anomalies remain unclear. Magma ocean crystallization is one possibility (Brown and Elkins-Tanton, 2009; Wang et al., 2022; Mouser and Dygert, 2023), but the dynamics of convection, melt production, and extraction in an initially radially heterogeneous mantle is complex (e.g., Tosi et al., 2013a) and does not straightforwardly lead to the inferred crustal structures. The question therefore remains open, primarily awaiting future measurements by the BepiColombo mission (Benkhoff et al., 2021), particularly those related to surface mineralogy (Rothery et al., 2020), which could provide new clues about the nature and origin of the high-Mg region.

Despite the low viscosity near the CMB where plumes form (see, e.g., Fig. 9b and f), in all analyzed cases, the planform of mantle convection is small-scale, with cells having a horizontal extent comparable to the thickness of the convective sublithospheric mantle. The cells are stable and undergo little horizontal movement, which confirms previous, but less general, findings (Tosi et al., 2015). This particular feature of the mantle flow, combined with the assumption of vertical melt extraction, leads to the peculiar pattern of crustal thickness observed in our models, where areas of thick crust over upwellings flank areas above downwellings where nearly no crust is produced (Fig. 5). This behavior is remarkably different from that of mantle convection in other planets such as Mars or Venus, where plumes undergo significant lateral movement that results in the formation of wide, contiguous regions of elevated crustal thickness (e.g., Keller and Tackley, 2009; Šrámek and Zhong, 2012; Tian et al., 2023).

In a thin mantle such as that of Mercury, where the growing stagnant lid can quickly reduce the thickness of the active layer to less than 300 km (Fig. 7c), it is natural to expect convection to be dominated by small spatial scales. A primordial compositional stratification, possibly followed by a mantle overturn (Brown and Elkins-Tanton, 2009; Mouser and Dygert, 2023), would lead to stably-stratified layers, which we did not considered here. These would further reduce the thickness of the convective part of the mantle (e.g., Tosi et al., 2013a), and in turn the spatial scale of convection. Basin-forming impacts could play a role, but their influence is limited in time and their effects on the dynamics of the mantle are not of global character (Roberts and Barnouin, 2012); they are expected to leave a surface signature at the spatial scale of the basin (Padovan et al., 2017).

Our assumption of vertical melt extraction, although commonly used, may be particularly strong for Mercury. While vertical melt motion is certainly important, the potential for lateral melt migration at depth (e.g., Rubin, 1995) and intrusive magmatism (Lourenço et al., 2020; Tian et al., 2023) may introduce feedback mechanisms, such as focusing of upwelling in areas of thickened crust, that could alter the crustal thickness patterns predicted by our models. These processes can redistribute melt laterally before it reaches the surface, potentially smoothing out and amplifying regional variations in crustal thickness. This effect could be particularly significant in regions where mantle plumes or localized heating occur (e.g., Plesa et al., 2016), leading to deviations from the patterns derived under the assumption of purely vertical melt extraction. Incorporating these lateral melt redistribution processes in future models may provide a better framework for reconciling the inferred crustal thickness anomalies with the dynamics of Mercury's interior.

Despite the above issues, our models generally predict average crustal thicknesses that are well compatible with the expectations based on gravity and topography data (∼15 to 60 km as discussed in Section 1.1). Fig. 13 summarizes our results showing, for each model, the final crust thickness after 1 Gyr as a function of the time at which crust production ends.

The choice of the internal heat production rate has the most clear influence on both the final crust thickness and the time at which this is achieved. Models incorporating low amounts of HPE yield low crust thicknesses around 15–20 km, with end times that do not exceed 650 Myr (blue symbols in Fig. 13). Models assuming an intermediate heat production generally result in crust thicknesses of ∼30–40 km and longer production times between 550 and 800 Myr (orange symbols in Fig. 13). However, for both model families, considering a variable thermal conductivity (blue and orange empty symbols in Fig. 13) has the clear effect of extending the time span of crust production, primarily as a consequence of the low thermal conductivity of the lithosphere (see Section 5.3). Models employing a EH-chondrites abundance of HPE result in crust production times up to ∼950 Myr (red symbols in Fig. 13).

Based on crater-size frequency distributions of the largest volcanic deposits and of the northern smooth plains, Byrne et al. (2016) proposed that the major phase of widespread effusive volcanism on Mercury ended around 3.5 Ga. Using this estimate as a constraint for the end time of crust production, we observe that simulations that assume the highest heat production rate can be generally considered successful (red symbols in Fig. 13). Nevertheless, when using an EH abundance of HPE and in contrast to the use of a CI abundance (Fig. 7), the choice of the surface temperature distribution influences the final average crustal thickness. In Fig. 13, models 26 and 29 use EH heat sources and 3:2 and 1:1 surface temperature distributions, respectively. The increased melt production caused by the combination of high HPE and (locally) high surface temperature ultimately leads to crust thicknesses of ∼80 km, much larger than 47 km produced when considering a constant surface temperature (simulation 25).

5.2. Evolution of radial contraction

We summarize in Fig. 14 our results on planetary contraction. For all models, the figure shows the total radius change after 1 Gyr of evolution as a function of the average rate of radius change measured either from the beginning until 1 Gyr (lower data series with red labels), or from 500 Myr until 1 Gyr (upper data series with black labels). For each point, the vertical error bars indicate the radius change associated with areas centered at the hot and cold poles (upper and lower limits,

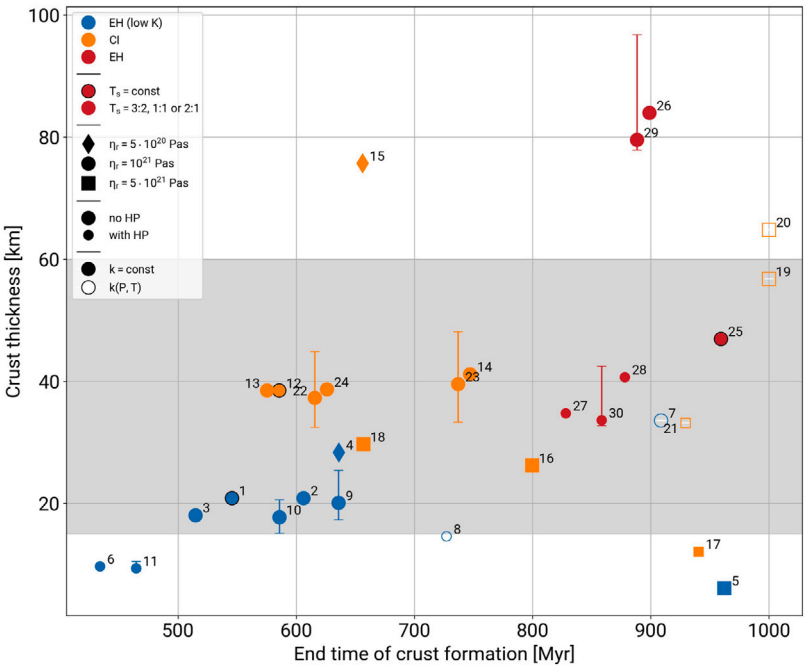

Fig. 13. Mean crust thickness after 1 Gyr for all models as a function of the time at which crust production ended. Each symbol corresponds to a specific simulation with parameters as indicated in the legend and simulation numbers as reported in Table 2. A range of variability is indicated only for cases assuming a 1:1 surface temperature, with the lower and upper bound corresponding to the crust thickness averaged beneath the cold and hot poles, respectively (see Section 2.5 for details). The gray area indicates the approximate range of average crust thickness (15–60 km) inferred from gravity and topography data. For models 19 and 20 (empty orange squares), the end time of crust production is artificially set at to 1000 Myr (i.e. the end of the computational time) although in these two cases, crust production would continue beyond this time (see red and orange lines in Fig. 11e). (For interpretation of the references to color in this figure legend, the reader is referred to the web version of this article.)

respectively) from simulations that employ non-uniform surface temperature distributions, while the horizontal error bars indicate the same but for the rate of radius change (right and left limits, respectively).

As for the evolution of the crust, the choice of the HPE model has the strongest influence also on radial contraction and its rate, which are largest for the low HPE model based on K-depleted EH chondrites (blue points in Fig. 14), intermediate for the CI model (orange points), and lowest for the EH model (red points), which has the highest heat production. This trend is offset when the reference viscosity is high and/or a variable thermal conductivity is used since both parameters tend to slow down mantle cooling (empty orange squares in Fig. 14).

Estimates of the global contraction accumulated until present and recorded by surface compressional features start from ~4 Ga, i.e. after the ~500-Myr-long initial phase of strong volcanic resurfacing that likely erased older geological structures (Marchi et al., 2013). The rates of radius change measured between 500 Myr and 1 Gyr (upper data series in Fig. 14) are only marginally affected by the uncertain thermal contributions due to the onset of convection, by crust production and, where considered, by heat piping. Therefore, since long-term mantle and core cooling decrease approximately linearly (e.g., Tosi et al., 2013), these rates can be extrapolated in time and compared with estimates based on the geological record (Byrne et al., 2014; Watters, 2021). The rate of radial contraction is ~4–5 km/Gyr for models with the lowest heat production (upper blue symbols in Fig. 14), ~3–4 km/Gyr for models with intermediate heat production (upper orange symbols), and ~1.5–2 km/Gyr for models with the highest heat production (upper red symbols). Considering an approximate contraction between 500 Myr and 1 Gyr of 2, 1.5 and 1 km, respectively, for the above three cases (as shown in Fig. 14), starting from 500 Myr and extrapolating the contraction rates to the present-day, we obtain total contractions of 16–19.5 km in the first case, 12–15.5 km in the second, and 6.25–8 km in the third. The last range is compatible with the estimates by Byrne et al. (2014) who proposed a radial contraction up to 7 km, but difficult to reconcile with those of Watters (2021) whose estimates are much lower (1–2 km) due to the neglect of small-scale compressive features that may be caused by local crust deformation rather than global contraction. Nevertheless, these models are also associated with crust thicknesses that exceed expectations (Fig. 13). As discussed in the following Section 5.3, considering the influence of heat piping, possibly in combination with a low thermal conductivity can help mitigate these issues.

Simulations assuming a surface temperature distribution associated with a synchronous rotation – and to a lesser extent with a 2:1 resonance – lead to hemispherical patterns of both crust thickness and radial contraction. An elevated crustal thickness and a reduced contraction characterize areas corresponding to the hottest parts of the surface, as opposed to a reduced crustal thickness and increased contraction away from these areas where the surface temperature is low. Different from the evolution of the crust for which it takes a few hundred million years to develop significant lateral differences in thickness (see e.g. Fig. 8b), radial contraction proceeds with a laterally heterogeneous rate already from the beginning of the evolution (see e.g. Fig. 8e). As shown by the vertical bars in Fig. 14, for the synchronous case, the difference in radial contraction between hot and cold poles after 1 Gyr can range from 1 km or less up to more than 3 km for the cases considering a K-depleted EH abundance of HPE. Despite the limitations of our models, we believe that these effects are robust and difficult to avoid. Particularly for the synchronous case, traces of the hemispherical character of contraction should have persisted until today if the resonance was maintained for an extended period of time. Therefore, the absence of a clear evidence for a hemispheric distribution of crust thickness and contractional features suggests that, if this resonance was ever attained, its lifetime probably did not reach 1 Gyr.

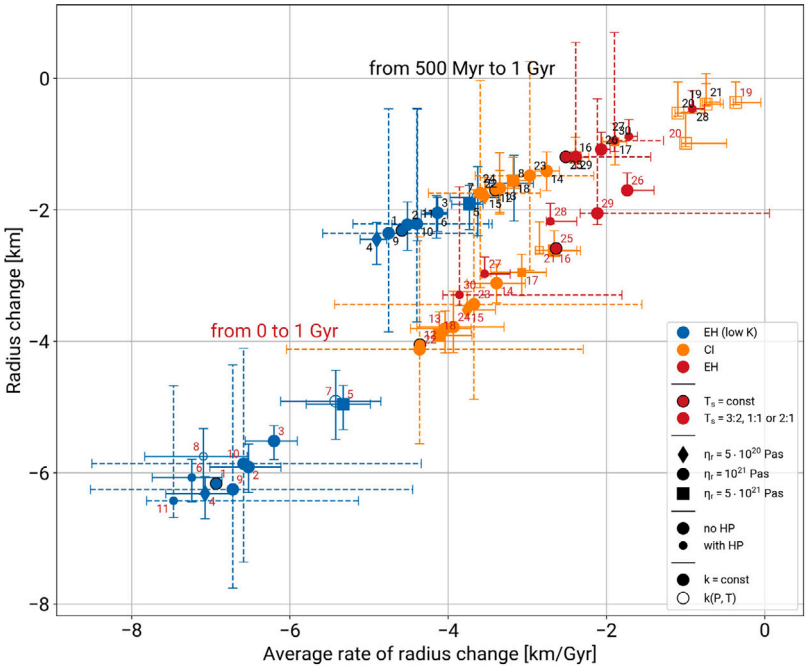

Fig. 14. Radius change after 1 Gyr computed since the beginning of the evolution (lower symbol series marked with red numbers and "from 0 to 1 Gyr") and between 500 Myr and 1 Gyr (upper symbol series marked with black numbers and "from 500 Myr to 1 Gyr") for all simulations as a function of the average rate of radius change measured over the two time intervals. A range of variability is indicated for all cases that consider a variable surface temperature (3:2, 1:1 or 2:1), with the lower and upper bounds that indicate the radius change corresponding to the hot and cold poles of the surface temperature distribution, and the right and left bounds indicating the rate of radius change for the same areas, respectively. Dashed error bars correspond to cases assuming a synchronous rotation, solid error bars to the other cases without distinction. (For interpretation of the references to color in this figure legend, the reader is referred to the web version of this article.)

Wieczorek et al. (2012) suggested that a synchronous rotation may have been present until ~3.7 Ga, at which time the impact that formed the Caloris basin possibly unlocked the early resonance. Assuming that the oldest surface record is 4 Gyr old, this would leave ~300 Myr of hemispheric contraction that the surface may have recorded. For example, over this time interval, for simulation n. 22 (red lines in Fig. 8), the difference in radial contraction between the cold and hot spots would be ~0.3 km. For the same case, but assuming a 2:1 resonance (simulation n. 24 and blue lines in Fig. 8), the difference would only be ~0.1 km. Whether such hemispheric differences are present in the record of contractional features remains unclear, but this could be a promising avenue for future research, particularly given the high-resolution imaging and topography data that the BepiColombo mission will provide (Rothery et al., 2020; Genova et al., 2021).

5.3. Importance of thermal and transport properties for crust production and radial contraction

The above effects of the HPE abundances on crust production and radial contraction can be modified by the choice of other model parameters, specifically by the reference viscosity, thermal conductivity, and consideration of the heat piping effect. Increasing the reference viscosity slows down mantle cooling and thickens the lithosphere, causing lower radial contraction and a thinner crust (compare e.g. simulations 2 and 5, or 13 and 16 in Figs. 13 and 14). Using a low thermal conductivity has a qualitatively similar effect on radial contraction, but also causes high mantle temperatures that result in long-lived partial melting and in the production of very thick crusts (compare models 16 and 19). The latter can be avoided by accounting for the influence of heat piping (compare models 20 and 21), which plays a critical role in reducing the thickness of the crust also in cases that consider a high heat production rate and a constant thermal conductivity (compare models 26 and 28). Using the lowest value of the reference viscosity ($5 \cdot 10^{20}$ Pa s) causes the stagnant lid to become thinner (Fig. 10c). It promotes melting at shallower depths and ultimately leads to a very thick crust (Fig. 10e), incompatible with the existing constraints. In addition, the cooling rate due to vigorous convection increases, causing more and more radial contraction (Fig. 10g), which attains values that vastly exceed the available constraints. Therefore, despite the limited range of reference viscosities that we considered, we anticipate that a further reduction of this parameter below $5 \cdot 10^{20}$ Pa s could hardly result in models compatible with the observations.

Determining a preferred model is not straightforward, but a few considerations can be made that can guide future efforts. Although the debate concerning the total amount of accumulated radial contraction is not settled, it is reasonable to expect values that fall between the two existing end-member estimates, namely between ~2 (Watters, 2021) and ~7 km (Byrne et al., 2014). Our results show that it is challenging to keep the total contraction accumulated over the evolution even below the upper end of the above range. As discussed also in Section 5.2, models using the highest heat production (EH model) could be compatible, with the resulting crust that would be too thick unless heat piping is also considered (compare simulations 26 and 27, or 29 and 30). An even lower radial contraction can be obtained upon considering the intermediate CI heat production together with a variable (i.e. low) thermal conductivity. Simulations 19 and 20, for example, accumulate about 0.5 km of contraction between 500 Myr and 1 Gyr and contract further at a rate of ~1 km/Gyr, with a total radius change until present of ~ − 4 km. For the same two models, crust production is still ongoing after 1 Gyr (i.e. at the end of the simulations), when it has reached ~60 km, thus indicating that these parameters tend to yield too thick crusts (>60 km) that are produced

for too long (>1 Gyr). Again, considering heat piping (simulation 21) helps solve these issues yielding similar contraction, but a remarkably lower crust thickness: ∼33 km after ∼920 Myr (see small orange square in Fig. 13). Models that satisfy the constraints on total contraction, mean crustal thickness and timing of crust production, however, are characterized by uniform rates of radius change after 500 Myr. Only during the first few hundred million years of evolution the rate of contraction tends to be higher as a consequence of the initial strong cooling due to the onset of thermal convection (see e.g. Fig. 7e or Fig. 10g and h). This aspect of the models remains difficult to reconcile with the idea that large-scale thrust systems formed early (e.g., Ferrari et al., 2015) and that radial contraction may have proceeded over time at a decreasing rate (Crane and Klimczak, 2017). Lithospheric cooling due to volcanism and heat piping have been proposed as possible mechanisms to enhance early contraction (Peterson et al., 2021), a feature that our models also show (see e.g. Fig. 11h). Yet, the phase during which this mechanism is most active overlaps with the early volcanic resurfacing and is difficult to extend beyond 500 Myr, i.e. the age of the oldest surface units, leaving thus open the possible causes of a time-variable rate of radial contraction.

6. Conclusions

We used 3D simulations of thermochemical mantle convection to investigate the influence of the surface temperature distributions caused by different early spin–orbit resonances on the first billion years of evolution of Mercury's interior, the period during which the planet experienced widespread volcanism and crust production (Byrne et al., 2016). We performed these simulations to search for a physically consistent mechanism able to generate the kind of large-scale lateral variations in crustal thickness that are expected from inversions of gravity and topography data (e.g., Smith et al., 2012; Genova et al., 2019; Beuthe et al., 2020). Additionally, we described the role of a number of key parameters – internal heat production, viscosity, thermal conductivity and expansivity, cooling via heat piping – that affect the interior evolution.

From a global-scale perspective, the thermal evolution and crust production are primarily controlled by the choice of the heat production rate, with intermediate to high bulk concentrations of heat producing elements (CI and EH models) delivering the most consistent results in terms of timing and volume of both crust production and radial contraction. Besides the mantle reference viscosity, considering the (usually-neglected) pressure and temperature dependence of the thermal conductivity strongly influences the evolution of the mantle temperature. The relatively low conductivity attained at Mercury's conditions slows down mantle cooling and enhances crust production, with modeled mean crustal thicknesses that can easily exceed values expected from gravity and topography data. This behavior, however, can be strongly offset by additionally considering the influence of lithosphere and crust cooling due to melt extraction and sedimentation, i.e. the so-called heat-piping effect.

The hemispheric surface temperature variations that accompany a 1:1 or 2:1 resonance cause increased melting and crust production beneath the hot hemisphere. In the synchronous case, when averaged laterally over wide areas, the crustal thickness variations produced by our models are marginally comparable in magnitude with those suggested by gravity and topography data. The hemispheric temperature perturbations strongly affect crust production, but remain superimposed to the small-scale convection pattern and essentially decoupled from it. Under the assumption of purely vertical melt extraction, the pattern of the modeled crust largely reflects the structure of the weakly time-dependent mantle convection, with thick crusts above hot upwellings and nearly no crust above cold downwellings. To make progress toward the self-consistent generation of crust thickness variations better comparable with those inferred from gravity and topography data, future models might need to include a more sophisticated treatment of melt extraction accounting for its lateral spreading at the surface and at depth.

At the largest spatial scales, the distribution of mantle temperature and crust thickness obtained in the 1:1 and 2:1 cases are also hemispherical, like the corresponding surface temperature. Although crustal thickness models do not readily support this pattern, the current knowledge of the surface composition and gravity field is relatively poor and largely limited to the northern hemisphere. Mineralogical mapping of the entire surface (Rothery et al., 2020) and high-resolution gravity field and topographic mapping by BepiColombo (Genova et al., 2021) will allow determining whether or not large-scale heterogeneities such as those associated with the high-Mg region and the underlying thick crust extend to the southern hemisphere, possibly providing a stronger support for our models.

Additionally to the crust, our models predict also radius changes due to thermal expansion and contraction to be hemispherical, with the hot hemisphere contracting less and at a slower rate than the cold hemisphere as long as the resonance is in place. Due to early global volcanic resurfacing, Mercury's geological record starts at ∼4 Ga (Marchi et al., 2013). If an early 1:1 resonance was unlocked by the Caloris impact at ∼3.7 Ga (Le Feuvre and Wieczorek, 2011; Wieczorek et al., 2012), the effects of hemispheric radial contraction could have accumulated at the surface for about 300 Myr, while hemispheric crust production would have continued for 800 Myr (i.e., roughly from the beginning of the evolution until the formation of the Caloris basin). The observational record does not clearly reveal evidence for such hemispheric evolution, which could imply that the resonance was significantly shorter-lived. Alternatively, future analyses using improved high-resolution data from the BepiColombo mission should be able to identify potential indicators of this process.

CRediT authorship contribution statement

Nicola Tosi: Writing – original draft, Visualization, Validation, Supervision, Software, Methodology, Investigation, Funding acquisition, Formal analysis, Data curation, Conceptualization. **Falko Schulz:** Writing – review & editing, Validation, Software, Methodology. **Michaela Walterová:** Writing – review & editing, Software, Methodology, Conceptualization. **Sebastiano Padovan:** Writing – review & editing, Software, Methodology, Conceptualization.

Declaration of competing interest

The authors declare that they have no known competing financial interests or personal relationships that could have appeared to influence the work reported in this paper.

Acknowledgments

We thank two anonymous reviewers for their thoughtful comments and suggestions, and Sean Raymond for editorial handling. Part of this work was supported by the German Research Foundation (DFG) (grant number TO TO 704/2-1).

Appendix. Supplementary figures

See Figs. A.1–A.4.

Data availability

A Jupyter Notebook and data to reproduce all the figures of the paper are available at https://zenodo.org/records/15484924.

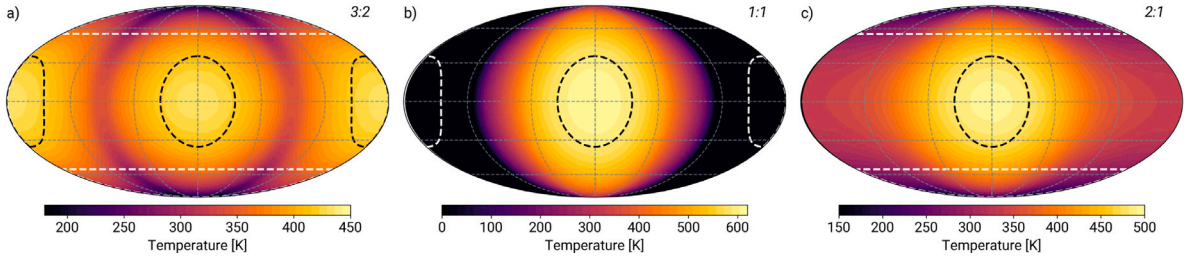

Fig. A.1. Time-averaged surface temperature distribution in the case of (a) 3:2, (b) 1:1, and (c) 2:1 spin–orbit resonances for an assumed eccentricity of 0.2 and a zero obliquity. The black and white dashed lines are circles with radii of 1500 km centered at the hottest and coldest spots of the respective surface temperature distributions.

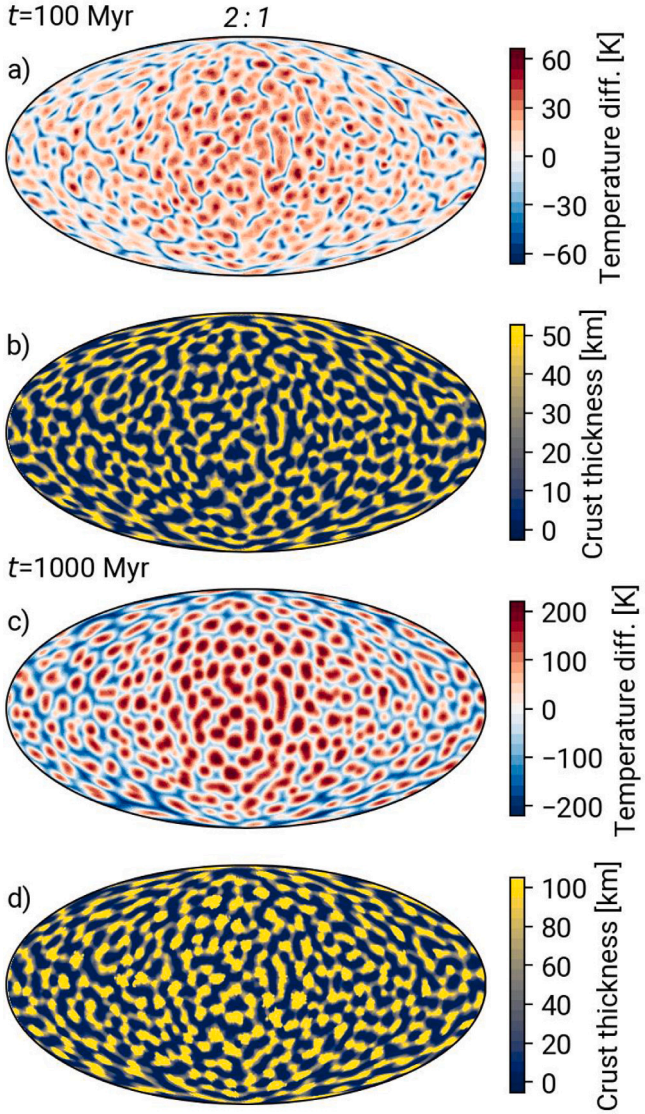

Fig. A.2. As in Fig. 5, upper mantle temperature anomalies and crustal thickness after 100 Myr (a,b) and 1000 Myr (c,d) of evolution based on CI abundance of heat producing elements and using the 2:1 surface temperature distribution (simulation 24).

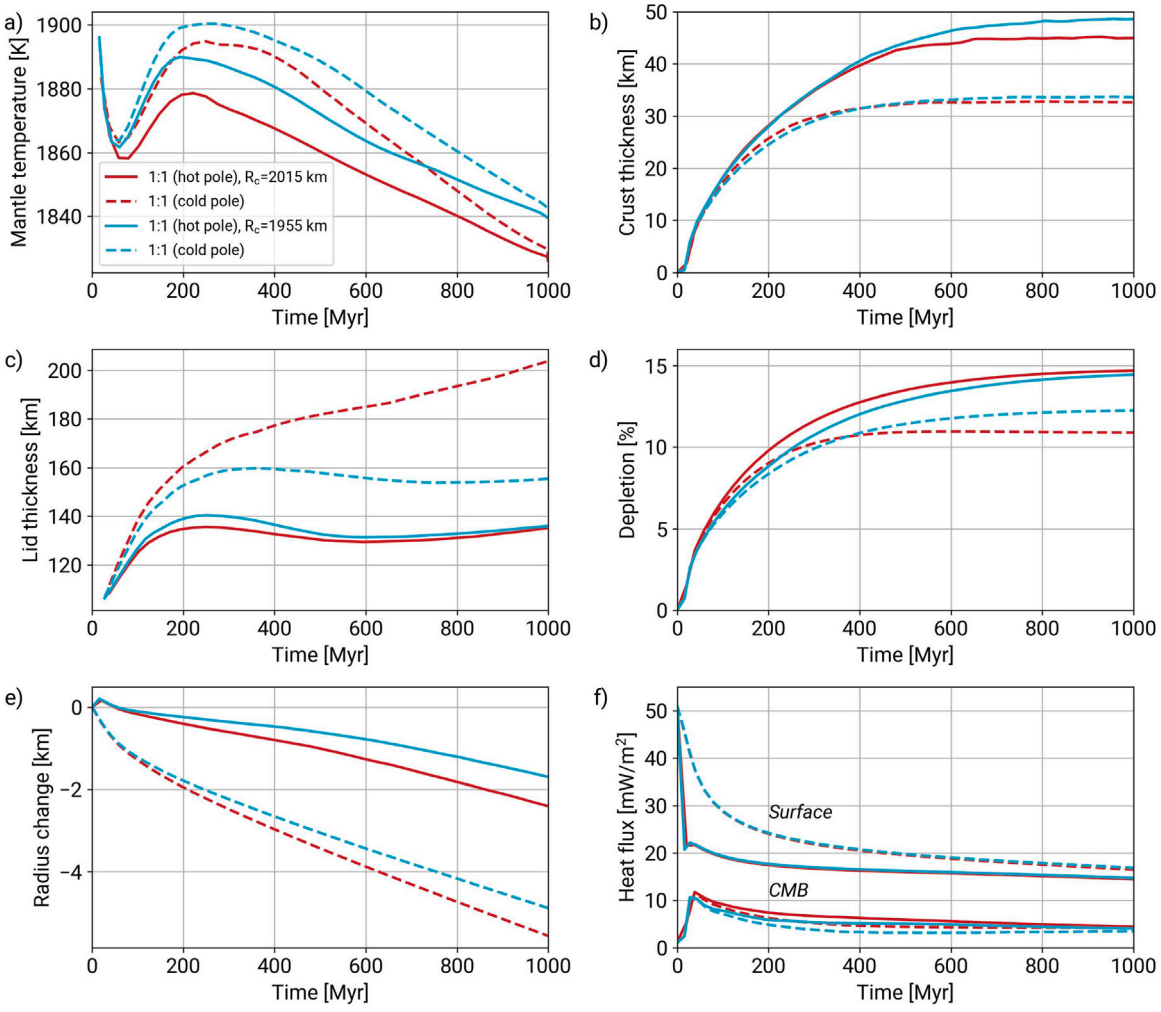

Fig. A.3. Timeseries of (a) volume-averaged sub-lid temperature, (b) crustal thickness, (c) stagnant lid thickness, (d) depletion, (e) radius change, and (f) surface and CMB heat fluxes for the 1:1 case and assuming a core radius of 2015 km (simulation 22 in Table 2 and red lines as in Fig. 8) and a smaller core radius of 1955 km (simulation 23 in Table 2 and cyan lines). All quantities are averaged over a circle with a radius of 1500 km centered where the surface temperature is highest (hot pole, solid lines) or lowest (cold pole, dashed lines). (For interpretation of the references to color in this figure legend, the reader is referred to the web version of this article.)

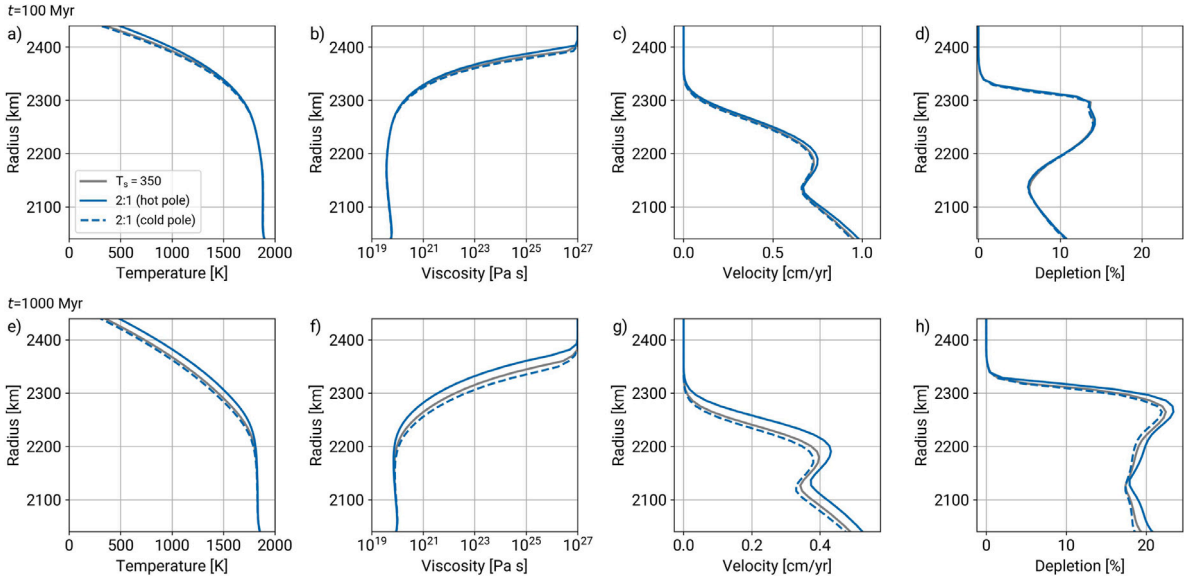

Fig. A.4. Radial profiles of temperature (a, e), viscosity (b, f), flow velocity (c, g) and depletion (d, h) after 100 Myr (top line) and 1000 Myr (bottom line) for the case with constant (simulation 12, gray lines) and 2:1 surface temperature distribution (simulation 24, blue lines) cases. Solid and dashed lines refer to profiles beneath the hot and cold poles, respectively. (For interpretation of the references to color in this figure legend, the reader is referred to the web version of this article.)

References

Agnor, C.B., Canup, R.M., Levison, H.F., 1999. On the character and consequences of large impacts in the late stage of terrestrial planet formation. Icarus 142 (1), 219–237. http://dx.doi.org/10.1006/icar.1999.6201.

Benkhoff, J., Murakami, G., Baumjohann, W., Besse, S., Bunce, E., Casale, M., Cremosese, G., Glassmeier, K.-H., Hayakawa, H., Heyner, D., et al., 2021. BepiColombo-mission overview and science goals. Space Sci. Rev. 217 (8), 90. http://dx.doi.org/10.1007/s11214-021-00861-4.

Beuthe, M., Charlier, B., Namur, O., Rivoldini, A., Van Hoolst, T., 2020. Mercury's crustal thickness correlates with lateral variations in mantle melt production. Geophys. Res. Lett. 47 (9), http://dx.doi.org/10.1029/2020GL087261.

Breuer, D., Hauck, S.A., Buske, M., Pauer, M., Spohn, T., 2007. Interior evolution of Mercury. Space Sci. Rev. 132 (2–4), 229–260. http://dx.doi.org/10.1007/s11214-007-9228-9.

Brown, S.M., Elkins-Tanton, L.T., 2009. Compositions of Mercury's earliest crust from magma ocean models. Earth Planet. Sci. Lett. 286 (3–4), 446–455. http://dx.doi.org/10.1016/j.epsl.2009.07.010.

Byrne, P.K., Klimczak, C., Şengör, C., Solomon, S.C., Watters, T.R., Hauck, II, S.A., 2014. Mercury's global contraction much greater than earlier estimates. Nat. Geosci. 7 (4), 301–307. http://dx.doi.org/10.1038/ngeo2097.

Byrne, P.K., Ostrach, L.R., Fassett, C.I., Chapman, C.R., Denevi, B.W., Evans, A.J., Klimczak, C., Banks, M.E., Head, J.W., Solomon, S.C., 2016. Widespread effusive volcanism on Mercury likely ended by about 3.5 Ga. Geophys. Res. Lett. 43 (14), 7408–7416. http://dx.doi.org/10.1002/2016GL069412.

Charlier, B., Grove, T.L., Zuber, M.T., 2013. Phase equilibria of ultramafic compositions on Mercury and the origin of the compositional dichotomy. Earth Planet. Sci. Lett. 363, 50–60. http://dx.doi.org/10.1016/j.epsl.2012.12.021.

Christensen, U.R., Yuen., D.A., 1984. Layered convection induced by phase transitions. J. Geophys. Res.: Solid Earth 90 (B12), 10291–10300. http://dx.doi.org/10.1029/JB090iB12p10291.

Correia, A.C.M., Laskar, J., 2012. Impact cratering on Mercury: Consequences for the spin evolution. Astrophys. J. Lett. 751 (2), http://dx.doi.org/10.1088/2041-8205/751/2/L43.

Crane, K.T., Klimczak, C., 2017. Timing and rate of global contraction on Mercury. Geophys. Res. Lett. 44 (7), 3082–3089. http://dx.doi.org/10.1002/2017GL072711.

Davies, C.J., Pommier, A., Greenwood, S., Wilson, A., 2024. Thermal and magnetic evolution of Mercury with a layered Fe-Si (-S) core. Earth Planet. Sci. Lett. 641, 118812. http://dx.doi.org/10.1016/j.epsl.2024.118812.

Denevi, B.W., Ernst, C.M., Meyer, H.M., Robinson, M.S., Murchie, S.L., Whitten, J.L., Head, J.W., Watters, T.R., Solomon, S.C., Ostrach, L.R., Chapman, C.R., Byrne, P.K., Klimczak, C., Peplowsk, P.N., 2013. The distribution and origin of smooth plains on Mercury. J. Geophys. Res.: Planets 118 (5), 891–907. http://dx.doi.org/10.1002/jgre.20075.

Ebel, D.S., Alexander, C.M.O., 2011. Equilibrium condensation from chondritic porous IDP enriched vapor: Implications for Mercury and enstatite chondrite origins. Planet. Space Sci. 59 (15), 1888–1894. http://dx.doi.org/10.1016/j.pss.2011.07.017.

Ferrari, S., Massironi, M., Marchi, S., Byrne, P.K., Klimczak, C., Martellato, E., Cremonese, G., 2015. Age relationships of the rembrandt basin and enterprise rupes, Mercury. Geol. Soc. Lond. Spec. Publ. 401 (1), 159–172. http://dx.doi.org/10.1144/sp401.20.

Fleury, A., Plesa, A.-C., Tosi, N., Walterová, M., Breuer, D., 2024. Variations of heat flux and elastic thickness of Mercury from 3-d thermal evolution modeling. Geophys. Res. Lett. 51 (21), e2024GL110622. http://dx.doi.org/10.1029/2024GL110622.

Genova, A., Goossens, S., Mazarico, E., Lemoine, F.G., Neumann, G.A., Kuang, W., Sabaka, T.J., Hauck, S.A., Smith, D.E., Solomon, S.C., Zuber, M.T., 2019. Geodetic evidence that Mercury has a solid inner core. Geophys. Res. Lett. 46 (7), 3625–3633. http://dx.doi.org/10.1029/2018GL081135.

Genova, A., Hussmann, H., Van Hoolst, T., Heyner, D., Iess, L., Santoli, F., Thomas, N., Cappuccio, P., Di Stefano, I., Kolhey, P., et al., 2021. Geodesy, geophysics and fundamental physics investigations of the BepiColombo mission. Space Sci. Rev. 217 (2), 31. http://dx.doi.org/10.1007/s11214-021-00808-9.

Giacomini, L., Massironi, M., Marchi, S., Fassett, C., Di Achille, G., Cremonese, G., 2015. Age dating of an extensive thrust system on Mercury: Implications for the planet's thermal evolution. Geol. Soc. Lond. Spec. Publ. 401 (1), 291–311. http://dx.doi.org/10.1144/SP401.21.

Goossens, S., Renaud, J.P., Henning, W.G., Mazarico, E., Bertone, S., Genova, A., 2022. Evaluation of recent measurements of Mercury's moments of inertia and tides using a comprehensive markov chain monte carlo method. Planet. Sci. J. 3 (2), 37. http://dx.doi.org/10.3847/PSJ/ac4bb8.

Grott, M., Breuer, D., Laneuville, M., 2011. Thermo-chemical evolution and global contraction of Mercury. Earth Planet. Sci. Lett. 307 (1), 135–146. http://dx.doi.org/10.1016/j.epsl.2011.04.040.

Guerrero, J.M., Lowman, J.P., Tackley, P.J., 2021. Did the cessation of convection in Mercury's mantle allow for a dynamo supporting increase in heat loss from its core? Earth Planet. Sci. Lett. 571, 117108. http://dx.doi.org/10.1016/j.epsl.2021.117108.

Guo, X., Feng, B., Zhang, B., Zhai, S., Xue, W., Song, Y., Song, Y., Yan, X., 2024. Effect of iron content on the thermal conductivity and thermal diffusivity of orthopyroxene. Geochem. Geophys. Geosyst. 25 (6), e2023GC011419. http://dx.doi.org/10.1029/2023GC011419.

Halbert, D., Parnell, J., 2022. Thermal conductivity of basalt between 225 and 290 K. http://dx.doi.org/10.1111/maps.13829.

Hauck, S.A., Dombard, A.J., Phillips, R.J., Solomon, S.C., 2004. Internal and tectonic evolution of Mercury. Earth Planet. Sci. Lett. 222 (3–4), 713–728. http://dx.doi.org/10.1016/j.epsl.2004.03.037.

Hauck, S.A., Grott, M., Byrne, B.P., Deneve, B.W., Stanley, S., McCoy, T.J., 2018. Mercury's global evolution. In: Solomon, S.C., Anderson, B.J., Nittler, L.R. (Eds.), Mercury, the View After MESSENGER. Cambridge University Press, pp. 516–543. http://dx.doi.org/10.1017/9781316650684.020.

Hauck, S.A., Margot, J.-L., Solomon, S.C., Phillips, R.J., Johnson, C.L., Lemoine, F.G., Mazarico, E., McCoy, T.J., Padovan, S., Peale, S.J., Perry, M.E., Smith, D.E., Zuber, M.T., 2013. The curious case of Mercury's internal structure. J. Geophys. Res.: Planets 118 (6), 1204–1220. http://dx.doi.org/10.1002/jgre.20091.

Hüttig, C., Tosi, N., Moore, W.B., 2013. An improved formulation of the incompressible Navier-Stokes equations with variable viscosity. Phys. Earth Planet. Inter. 220, 11–18. http://dx.doi.org/10.1016/j.pepi.2013.04.002.

Jain, C., Solomatov, V.S., 2024. Analysis of the cessation of convection in Mercury's mantle. J. Geophys. Res.: Planets 129 (9), e2024JE008365. http://dx.doi.org/10.1029/2024JE008365.

Karato, S.-i., Wu, P., 1993. Rheology of the upper mantle: A synthesis. Science 260 (5109), 771–778. http://dx.doi.org/10.1126/science.260.5109.771.

Keller, T., Tackley, P.J., 2009. Towards self-consistent modeling of the martian dichotomy: The influence of one-ridge convection on crustal thickness distribution. Icarus 202 (2), 429–443. http://dx.doi.org/10.1016/j.icarus.2009.03.029.

King, S.D., Lee, C., van Keken, P.E., Leng, W., Zhong, S., Tan, E., Tosi, N., Kameyama, M.C., 2010. A community benchmark for 2-D cartesian compressible convection in the Earth's mantle. Geophys. J. Int. 180 (1), 73–87. http://dx.doi.org/10.1111/j.1365-246X.2009.04413.x.

Kirk, R.L., Stevenson, D.J., 1989. The competition between thermal contraction and differentiation in the stress history of the moon. J. Geophys. Res.: Solid Earth 94 (B9), 12133–12144. http://dx.doi.org/10.1029/JB094iB09p12133.

Klima, R.L., Denevi, B.W., Ernst, C.M., Murchie, S.L., Peplowski, P.N., 2018. Global distribution and spectral properties of low-reflectance material on Mercury. Geophys. Res. Lett. 45 (7), 2945–2953. http://dx.doi.org/10.1002/2018GL077544.

Knibbe, J.S., Van Hoolst, T., 2021. Modelling of thermal stratification at the top of a planetary core: Application to the cores of Earth and Mercury and the thermal coupling with their mantles. Phys. Earth Planet. Inter. 321, 106804. http://dx.doi.org/10.1016/j.pepi.2021.106804.

Knibbe, J.S., van Westrenen, W., 2017. On Mercury's past rotation, in light of its large craters. Icarus 281, 1–18. http://dx.doi.org/10.1016/j.icarus.2016.08.036.

Knibbe, J.S., van Westrenen, W., 2018. The thermal evolution of Mercury's Fe–Si core. Earth Planet. Sci. Lett. 482, 147–159. http://dx.doi.org/10.1016/j.pepi.2021.106804.

Kokubo, E., Ida, S., 2007. Formation of terrestrial planets from protoplanets. II. Statistics of planetary spin. Astrophys. J. 671 (2), 2082. http://dx.doi.org/10.1086/522364.

Lark, L.H., Head, J.W., Huber, C., 2023. Evidence for a carbon-rich Mercury from the distribution of low-reflectance material (LRM) associated with large impact basins. Earth Planet. Sci. Lett. 613, 118192. http://dx.doi.org/10.1016/j.epsl.2023.118192.

Le Feuvre, M., Wieczorek, M.A., 2011. Nonuniform cratering of the Moon and a revised crater chronology of the inner Solar System. Icarus 214 (1), 1–20. http://dx.doi.org/10.1016/j.icarus.2011.03.010.

Ledlow, M.J., Burns, J.O., Gisler, G.R., Zhao, J.-H., Zeilik, M., Baker, D.N., 1992. Subsurface emissions from Mercury: VLA radio observations at 2 and 6 centimeters. Astrophys. J. 384, 640. http://dx.doi.org/10.1086/170906.

Li, L., Wentzcovitch, R.M., Weidner, D.J., da Silva, C.R.S., 2007. Vibrational and thermodynamic properties of forsterite at mantle conditions. J. Geophys. Res. (Solid Earth) 112 (B5), B05206. http://dx.doi.org/10.1029/2006JB004546.

Lourenço, D.L., Rozel, A.B., Ballmer, M.D., Tackley, P.J., 2020. Plutonic-squishy lid: A new global tectonic regime generated by intrusive magmatism on earth-like planets. Geochem. Geophys. Geosyst. 21 (4), e2019GC008756. http://dx.doi.org/10.1029/2019GC008756.

Man, B., Rothery, D.A., Balme, M.R., Conway, S.J., Wright, J., 2023. Widespread small grabens consistent with recent tectonism on Mercury. Nat. Geosci. 16 (10), 856–862. http://dx.doi.org/10.1038/s41561-023-01281-5.

Marchi, S., Chapman, C.R., Fassett, C.I., Head, J.W., Bottke, W., Strom, R.G., 2013. Global resurfacing of Mercury 4.0–4.1 billion years ago by heavy bombardment and volcanism. Nature 499 (7456), 59–61. http://dx.doi.org/10.1038/nature12280.

Margot, J., Hauck, S.A., Mazarico, E., Padovan, S., Peale, S.J., 2018. Mercury's internal structure. In: Solomon, S.C., Anderson, B.J., Nittler, L.R. (Eds.), Mercury, the View After MESSENGER. Cambridge University Press, pp. 85–113. http://dx.doi.org/10.1017/9781316650684.005.

Mazarico, E., Genova, A., Goossens, S., Lemoine, F.G., Neumann, G.A., Zuber, M.T., Smith, D.E., Solomon, S.C., 2014. The gravity field, orientation, and ephemeris of Mercury from MESSENGER observations after three years in orbit. J. Geophys. Res.: Planets 119 (12), 2417–2436. http://dx.doi.org/10.1002/2014JE004675.

McCoy, T.J., Peplowski, P.N., McCubbin, F.M., Weider, S.Z., 2018. The geochemical and mineralogical diversity of Mercury. In: Solomon, S.C., Nittler, L.R., Anderson, B.J. (Eds.), Mercury. the View After MESSENGER. pp. 176–190. http://dx.doi.org/10.1017/9781316650684.008.

McDonough, W.F., Sun, S.-s., 1995. The composition of the Earth. Chem. Geol. 120 (3–4), 223–253. http://dx.doi.org/10.1016/0009-2541(94)00140-4.

Meier, T.G., Bower, D.J., Lichtenberg, T., Hammond, M., Tackley, P.J., Pierrehumbert, R.T., Caballero, J.A., Tsai, S.-M., Weiner Mansfield, M., Tosi, N., et al., 2024. Geodynamics of super-earth GJ 486b. J. Geophys. Res.: Planets 129 (10), e2024JE008491. http://dx.doi.org/10.1029/2024JE008491.

Michel, N.C., Hauck, S.A., Solomon, S.C., Phillips, R.J., Roberts, J.H., Zuber, M.T., 2013. Thermal evolution of Mercury as constrained by MESSENGER observations. J. Geophys. Res.: Planets 118 (5), 1033–1044. http://dx.doi.org/10.1002/jgre.20049.

Miguel, Y., Brunini, A., 2010. Planet formation: Statistics of spin rates and obliquities of extrasolar planets. Mon. Not. R. Astron. Soc. 406 (3), 1935–1943. http://dx.doi.org/10.1111/j.1365-2966.2010.16804.x.

Mitchell, D.L., de Pater, I., 1994. Microwave imaging of Mercury's thermal emission at wavelengths from 0.3 to 20.5 cm. Icarus 110 (1), 2–32. http://dx.doi.org/10.1006/icar.1994.1105.

Moore, W.B., Webb, A.A.G., 2013. Heat-pipe Earth. Nature 501 (7468), 501–505. http://dx.doi.org/10.1038/nature12473.

Mouser, M.D., Dygert, N., 2023. On the potential for cumulate mantle overturn in Mercury. J. Geophys. Res.: Planets 128 (7), e2023JE007739. http://dx.doi.org/10.1029/2023JE007739.

Namur, O., Charlier, B., 2017. Silicate mineralogy at the surface of Mercury. Nat. Geosci. 10 (1), 9–13. http://dx.doi.org/10.1038/ngeo2860.

Namur, O., Collinet, M., Charlier, B., Grove, T.L., Holtz, F., McCammon, C., 2016. Melting processes and mantle sources of lavas on Mercury. Earth Planet. Sci. Lett. 439, 117–128. http://dx.doi.org/10.1016/j.epsl.2016.01.030.

Nittler, L.R., Starr, R.D., Weider, S.Z., McCoy, T.J., Boynton, W.V., Ebel, D.S., Ernst, C.M., Evans, L.G., Goldsten, J.O., Hamara, D.K., Lawrence, D.J., McNutt, R.L., Schlemm, C.E., Solomon, S.C., Sprague, A.L., 2011. The major-element composition of Mercury's surface from MESSENGER X-ray spectrometry. Science 333 (6051), 1847. http://dx.doi.org/10.1126/science.1211567.

Noyelles, B., Frouard, J., Makarov, V.V., Efroimsky, M., 2014. Spin-orbit evolution of Mercury revisited. Icarus 241, 26–44. http://dx.doi.org/10.1016/j.icarus.2014.05.045.

Orgel, C., Fassett, C.I., Michael, G., Riedel, C., van der Bogert, C.H., Hiesinger, H., 2020. Re-examination of the population, stratigraphy, and sequence of mercurian basins: Implications for Mercury's early impact history and comparison with the Moon. J. Geophys. Res.: Planets 125 (8), e06212. http://dx.doi.org/10.1029/2019JE006212.

Padovan, S., Tosi, N., Plesa, A.-C., Ruedas, T., 2017. Impact-induced changes in source depth and volume of magmatism on Mercury and their observational signatures. Nat. Commun. 8, 1945. http://dx.doi.org/10.1038/s41467-017-01692-0.

Padovan, S., Wieczorek, M.A., Margot, J.-L., Tosi, N., Solomon, S.C., 2015. Thickness of the crust of Mercury from geoid-to-topography ratios. Geophys. Res. Lett. 42 (4), 1029–1038. http://dx.doi.org/10.1002/2014GL062487.

Peplowski, P.N., Klima, R.L., Lawrence, D.J., Ernst, C.M., Denevi, B.W., Frank, E.A., Goldsten, J.O., Murchie, S.L., Nittler, L.R., Solomon, S.C., 2016. Remote sensing evidence for an ancient carbon-bearing crust on Mercury. Nat. Geosci. 9 (4), 273–276. http://dx.doi.org/10.1038/ngeo2669.

Peplowski, P.N., Lawrence, D.J., Rhodes, E.A., Sprague, A.L., McCoy, T.J., Denevi, B.W., Evans, L.G., Head, J.W., Nittler, L.R., Solomon, S.C., Stockstill-Cahill, K.R., Weider, S.Z., 2012. Variations in the abundances of potassium and thorium on the surface of Mercury: Results from the MESSENGER Gamma-ray spectrometer. J. Geophys. Res.: Planets 117, e00L04. http://dx.doi.org/10.1029/2012JE004141.

Peplowski, P.N., Stockstill-Cahill, K., 2019. Analytical identification and characterization of the major geochemical terranes of Mercury's northern hemisphere. J. Geophys. Res.: Planets 124 (9), 2414–2429. http://dx.doi.org/10.1029/2019JE005997.

Peterson, G.A., Johnson, C.L., Jellinek, A.M., 2021. Thermal evolution of Mercury with a volcanic heat-pipe flux: Reconciling early volcanism, tectonism, and magnetism. Sci. Adv. 7 (40), eabh2482. http://dx.doi.org/10.1126/sciadv.abh2482.

Pirotte, H., Cartier, C., Namur, O., Pommier, A., Zhang, Y., Berndt, J., Klemme, S., Charlier, B., 2023. Internal differentiation and volatile budget of Mercury inferred from the partitioning of heat-producing elements at highly reduced conditions. Icarus (ISSN: 0019-1035) 405, 115699. http://dx.doi.org/10.1016/j.icarus.2023.115699.

Plesa, A.C., Breuer, D., 2014. Partial melting in one-plate planets: Implications for thermo-chemical and atmospheric evolution. Planet. Space Sci. 98, 50–65. http://dx.doi.org/10.1016/j.pss.2013.10.007.

Plesa, A.-C., Grott, M., Tosi, N., Breuer, D., Spohn, T., Wieczorek, M., 2016. How large are present-day heat flux variations across the surface of Mars? J. Geophys. Res.: Planets 121 (12), 2386–2403.

Plesa, A.-C., Tosi, N., Hüttig, C., 2013. Thermo-chemical convection in planetary mantles: Advection methods and magma ocean overturn simulations. In: Rückemann, C.-P. (Ed.), Integrated Information and Computing Systems for Natural, Spatial, and Social Sciences. IGI Global, pp. 302–323. http://dx.doi.org/10.4018/978-1-4666-2190-9.ch015.

Rivoldini, A., Beuthe, M., Van Hoolst, T., 2010. Past and present tidal dissipation in Mercury. In: European Planetary Science Congress 2010.

Roberts, J.H., Barnouin, O.S., 2012. The effect of the caloris impact on the mantle dynamics and volcanism of Mercury. J. Geophys. Res.: Planets 117 (E2), http://dx.doi.org/10.1029/2011JE003876.

Rothery, D.A., Massironi, M., Alemanno, G., Barraud, O., Besse, S., Bott, N., Brunetto, R., Bunce, E., Byrne, P., Capaccioni, F., et al., 2020. Rationale for BepiColombo studies of Mercury's surface and composition. Space Sci. Rev. 216, 1–46. http://dx.doi.org/10.1007/s11214-020-00694-7.

Rubin, A.M., 1995. Propagation of magma-filled cracks. Annu. Rev. Earth Planet. Sci. 23, 287–336. http://dx.doi.org/10.1146/annurev.ea.23.050195.001443.

Schulz, F., Tosi, N., Plesa, A.-C., Breuer, D., 2020. Stagnant-lid convection with diffusion and dislocation creep rheology: Influence of a non-evolving grain size. Geophys. J. Int. 220 (1), 18–36. http://dx.doi.org/10.1093/gji/ggz417.

Smith, D.E., Zuber, M.T., Phillips, R.J., Solomon, S.C., Hauck, S.A., Lemoine, F.G., Mazarico, E., Neumann, G.A., Peale, S.J., Margot, J.-L., Johnson, C.L., Torrence, M.H., Perry, M.E., Rowlands, D.D., Goossens, S., Head, J.W., Taylor, A.H., 2012. Gravity field and internal structure of Mercury from MESSENGER. Science 336 (6078), 214. http://dx.doi.org/10.1126/science.1218809.

Sori, M.M., 2018. A thin, dense crust for Mercury. Earth Planet. Sci. Lett. 489, 92–99. http://dx.doi.org/10.1016/j.epsl.2018.02.033.

Šrámek, O., Zhong, S., 2012. Martian crustal dichotomy and tharsis formation by partial melting coupled to early plume migration. J. Geophys. Res.: Planets 117 (E1), http://dx.doi.org/10.1029/2011JE003867.

Tian, J., Tackley, P.J., Lourenço, D.L., 2023. The tectonics and volcanism of venus: New modes facilitated by realistic crustal rheology and intrusive magmatism. Icarus 399, 115539. http://dx.doi.org/10.1016/j.icarus.2023.115539.

Tosi, N., Grott, M., Plesa, A.C., Breuer, D., 2013. Thermochemical evolution of Mercury's interior. J. Geophys. Res.: Planets 118 (12), 2474–2487. http://dx.doi.org/10.1002/jgre.20168.

Tosi, N., Padovan, S., 2021. Mercury, Moon, Mars: Surface expression of mantle convection and interior evolution of stagnantli-lid bodies. In: Marquardt, H., Ballmer, M., Cottaar, S., Konter, J. (Eds.), Mantle Convection and Surface Expressions. American Geophysical Union, pp. 455–489. http://dx.doi.org/10.1002/9781119528609.ch17.

Tosi, N., Plesa, A.-C., Breuer, D., 2013a. Overturn and evolution of a crystallized magma ocean: A numerical parameter study for mars. J. Geophys. Res.: Planets 118 (7), 1512–1528. http://dx.doi.org/10.1002/jgre.20109.

Tosi, N., Čadek, O., Běhounková, M., Káňová, M., Plesa, A.C., Grott, M., Breuer, D., Padovan, S., Wieczorek, M.A., 2015. Mercury's low-degree geoid and topography controlled by insolation-driven elastic deformation. Geophys. Res. Lett. 42 (18), 7327–7335. http://dx.doi.org/10.1002/2015GL065314.

Tosi, N., Yuen, D.A., de Koker, N., Wentzcovitch, R.M., 2013b. Mantle dynamics with pressure-and temperature-dependent thermal expansivity and conductivity. Phys. Earth Planet. Inter. 217, 48–58. http://dx.doi.org/10.1016/j.pepi.2013.02.004.

Van Summeren, J., Conrad, C.P., Gaidos, E., 2011. Mantle convection, plate tectonics, and volcanism on hot exo-earths. Astrophys. J. Lett. 736 (1), L15. http://dx.doi.org/10.1088/2041-8205/736/1/L15.

Vander Kaaden, K.E., McCubbin, F.M., 2015. Exotic crust formation on Mercury: Consequences of a shallow, FeO-poor mantle. J. Geophys. Res.: Planets 120 (2), 195–209. http://dx.doi.org/10.1002/2014JE004733.

Vasavada, A.R., Paige, D.A., Wood, S.E., 1999. Near-surface temperatures on Mercury and the moon and the stability of polar ice deposits. Icarus (ISSN: 0019-1035) 141 (2), 179–193. http://dx.doi.org/10.1006/icar.1999.6175.

Wang, Y., Xiao, Z., Xu, R., 2022. Multiple mantle sources of high-magnesium terranes on Mercury. J. Geophys. Res.: Planets 127 (5), e2022JE007218. http://dx.doi.org/10.1029/2022JE007218.

Wang, C., Yoneda, A., Osako, M., Ito, E., Yoshino, T., Jin, Z., 2014. Measurement of thermal conductivity of omphacite, jadeite, and diopside up to 14 GPa and 1000 K: Implication for the role of eclogite in subduction slab. J. Geophys. Res.: Solid Earth 119 (8), 6277–6287. http://dx.doi.org/10.1002/2014JB011208.

Wasson, J.T., Kallemeyn, G.W., 1988. Compositions of chondrites. Phil. Trans. R. Soc. Lond. A (ISSN: 0019-1035) 325 (2), 535–544. http://dx.doi.org/10.1098/rsta.1988.0066.

Watters, T.R., 2021. A case for limited global contraction of Mercury. Commun. Earth & Environ. 2 (1), 9. http://dx.doi.org/10.1038/s43247-020-00076-5.

Weider, S.Z., Nittler, L.R., Starr, R.D., Crapster-Pregont, E.J., Peplowski, P.N., Denevi, B.W., Head, J.W., Byrne, P.K., Hauck, S.A., Ebel, D.S., Solomon, S.C., 2015. Evidence for geochemical terranes on Mercury: Global mapping of major elements with MESSENGER's X-Ray spectrometer. Earth Planet. Sci. Lett. 416, 109–120. http://dx.doi.org/10.1016/j.epsl.2015.01.023.

Weider, S.Z., Nittler, L.R., Starr, R.D., McCoy, T.J., Stockstill-Cahill, K.R., Byrne, P.K., Denevi, B.W., Head, J.W., Solomon, S.C., 2012. Chemical heterogeneity on Mercury's surface revealed by the MESSENGER X-Ray spectrometer. J. Geophys. Res.: Planets 117, e00L05. http://dx.doi.org/10.1029/2012JE004153.

Wieczorek, M.W., 2015. Gravity and topography of the terrestrial planets. In: Schubert, G. (Ed.), Treatise on Geophysics, second ed. Elsevier, pp. 153–193. http://dx.doi.org/10.1016/B978-0-444-53802-4.00169-X.

Wieczorek, M.A., Correia, A.C.M., Le Feuvre, M., Laskar, J., Rambaux, N., 2012. Mercury's spin-orbit resonance explained by initial retrograde and subsequent synchronous rotation. Nat. Geosci. 5 (1), 18–21. http://dx.doi.org/10.1038/ngeo1350.

Wieczorek, M.A., Meschede, M., 2018. SHTools: Tools for working with spherical harmonics. Geochem. Geophys. Geosyst. 19 (8), 2574–2592. http://dx.doi.org/10.1029/2018GC007529.

Wieczorek, M.A., Meschede, M., Brugere, T., Corbin, A., Hattori, A., Leinweber, K., Oshchepkov, I., Reinecke, M., Sales de Andrade, E., Schnetter, E., Schröder, S., Vasishta, A., Walker, A., Xu, B., Sierra, J., 2022. SHTools. http://dx.doi.org/10.5281/zenodo.592762, https://zenodo.org/records/6497293.

Xie, J.-C., Zhang, M., Huang, C.-L., 2022. Influence of megaregolith on the thermal evolution of Mercury's silicate shell. Res. Astron. Astrophys. 22 (3), http://dx.doi.org/10.1088/1674-4527/ac4ca1.

Xu, Y., Shankland, T.J., Linhardt, S., Rubie, D.C., Langenhorst, F., Klasinski, K., 2004. Thermal diffusivity and conductivity of olivine, wadsleyite and ringwoodite to 20 GPa and 1373 k. Phys. Earth Planet. Inter. 143, 321–336. http://dx.doi.org/10.1016/j.pepi.2004.03.005.

Zhang, Y., Yoshino, T., Yoneda, A., Osako, M., 2019. Effect of iron content on thermal conductivity of olivine with implications for cooling history of rocky planets. Earth Planet. Sci. Lett. 519, 109–119. http://dx.doi.org/10.1016/j.epsl.2019.04.048.

Zolotov, M.Y., Sprague, A.L., Hauck, S.A., Nittler, L.R., Solomon, S.C., Weider, S.Z., 2013. The redox state, FeO content, and origin of sulfur-rich magmas on Mercury. J. Geophys. Res.: Planets 118 (1), 138–146. http://dx.doi.org/10.1029/2012JE004274.